

1   **Quantitative *in vivo* analyses reveal a complex pharmacogenomic landscape in**  
2   **lung adenocarcinoma**

3  
4  
5  
6  
7   **Authors:**

8   Chuan Li<sup>1,9</sup>, Wen-Yang Lin<sup>2,9</sup>, Hira Rizvi<sup>3</sup>, Hongchen Cai<sup>2</sup>, Christopher D. McFarland<sup>1</sup>, Zoë N.  
9   Rogers<sup>2</sup>, Maryam Yousefi<sup>2</sup>, Ian P. Winters<sup>2</sup>, Charles M. Rudin<sup>4,5</sup>, Dmitri A. Petrov<sup>1,6\*</sup> and Monte  
10   M. Winslow<sup>2,6,7,8\*</sup>

11   **Affiliations:**

12   <sup>1</sup> Department of Biology, Stanford University, Stanford, CA, USA

13   <sup>2</sup> Department of Genetics, Stanford University School of Medicine, Stanford, CA, USA

14   <sup>3</sup> Druckenmiller Center for Lung Cancer Research, Memorial Sloan Kettering Cancer Center, New York, USA

15   <sup>4</sup> Department of Medicine, Thoracic Oncology Service, Memorial Sloan Kettering Cancer Center, New York, USA

16   <sup>5</sup> Department of Medicine, Weill Cornell Medical College, New York, USA

17   <sup>6</sup> Cancer Biology Program, Stanford University School of Medicine, Stanford, CA, USA

18   <sup>7</sup> Department of Pathology, Stanford University School of Medicine, Stanford, CA, USA

19   <sup>8</sup> Stanford Cancer Institute, Stanford University School of Medicine, Stanford, CA, USA

20   <sup>9</sup> These authors contributed equally

21

22   \* Corresponding authors:

23   Monte M. Winslow, Stanford University School of Medicine | 279 Campus Drive, Beckman Center, Room B256, Stanford, CA  
24   94305. Phone: 650-725-8696 | Fax: 650-725-1534 | E-mail: [mwinslow@stanford.edu](mailto:mwinslow@stanford.edu)

25

26   Dmitri A. Petrov, Stanford University | 327 Campus Drive, Bass Biology, Room 232, Stanford, CA 94305

27   Phone: 650-736-1169 | Fax: 650-723-6132| E-mail: [dpetrov@stanford.edu](mailto:dpetrov@stanford.edu)

28

29

30

31    **Abstract:**

32    The lack of knowledge about the relationship between tumor genotypes and therapeutic  
33    responses remains one of the most important gaps in enabling the effective use of cancer  
34    therapies. Here, we couple a multiplexed and quantitative platform with robust statistical  
35    methods to enable pharmacogenomic mapping of lung cancer treatment responses *in vivo*. We  
36    uncover a surprisingly complex map of genotype-specific therapeutic responses, with over 20%  
37    of possible interactions showing significant resistance or sensitivity. We validate one of these  
38    interactions - the resistance of Keap1 mutant tumors to platinum therapy - using a large patient  
39    response dataset. Our results highlight the importance of understanding the genetic determinants  
40    of treatment responses in the development of precision therapies and define a strategy to identify  
41    such determinants.

42

43    **Main Text:**

44         Efforts over the past decade have generated many novel cancer therapies. However, the  
45    lack of understanding of the relationship between tumor genotype and therapeutic response  
46    remains a major challenge in translating these therapies into precision cancer treatments <sup>1</sup>. While  
47    the genetic complexity of human cancer could in principle thwart therapeutic efforts that  
48    disregard biomarker-driven patient selection, it remains unclear the extent to which tumor  
49    suppressor gene alterations impact therapeutic responses <sup>2</sup>. Precisely mapping the  
50    pharmacogenomic landscape should help design better clinical trials and select more effective  
51    therapies for individual patients.

52         The pharmacogenomic landscape of cancer drug responses has been investigated using  
53    cell lines, patient-derived xenografts (PDXs), and patients themselves <sup>3-6</sup>. However, cell lines

54 grown *in vitro* lack the appropriate *in vivo* environment and the genotypic heterogeneity of  
55 patient tumors. PDXs and human cell line transplantation models recapitulate some aspects of *in*  
56 *vivo* growth, but growth factor/receptor incompatibility, growth in non-orthotopic sites, and the  
57 obligate absence of the adaptive immune system compromise these approaches<sup>7-9</sup>. Furthermore,  
58 human tumor-derived systems almost invariably have large numbers of mutations and genomic  
59 rearrangements, and thus even large-scale analyses often lack the statistical power to glean  
60 cause-and-effect relationships between individual genetic alterations and therapeutic responses  
61<sup>3,10</sup>.

62 Genetically engineered mouse models of cancer uniquely enable the introduction of  
63 defined genetic alterations into adult somatic cells, which leads to the generation of  
64 autochthonous tumors<sup>11</sup>. These tumors can recapitulate the genomic alterations, gene expression  
65 state, histopathology, and therapy-refractive nature of corresponding human cancers<sup>12,13</sup>. Despite  
66 the potential value of these models in pre-clinical translation studies, the breadth of their utility  
67 has been limited by the fact that they are neither readily scalable nor sufficiently quantitative<sup>14</sup>.

68 To increase the scope and precision of *in vivo* cancer modeling and to assess tumor  
69 suppressor gene function in a multiplexed manner, we recently developed a method based on  
70 tumor-barcoding coupled with high-throughput barcode sequencing (Tuba-seq). This method  
71 integrates CRISPR/Cas9-based somatic genome engineering and molecular barcoding into well-  
72 established Cre/Lox-based genetically engineered mouse models of oncogenic Kras-driven lung  
73 cancer<sup>14</sup>. The initiation of lung tumors with pools of barcoded Lenti-sgRNA/Cre viral vectors  
74 enables the generation of many tumors of different genotypes in parallel. All neoplastic cells  
75 within each clonal tumor have the same two-component barcode, where each sgID region  
76 identifies the sgRNA and the random barcode (BC) is unique to each tumor. Subsequent high-

77 throughput sequencing of the sgID-BC region from bulk tumor-bearing lungs can quantify the  
78 number of neoplastic cells in each tumor of each genotype.

79 We initiated lung tumors in *Kras*<sup>LSL-G12D/+</sup>; *Rosa26*<sup>LSL-Tomato</sup>; *H11*<sup>LSL-Cas9</sup> (*KT*; *H11*<sup>LSL-Cas9</sup>)  
80 mice and control Cas9-negative *KT* mice with a pool of barcoded Lenti-sgRNA/Cre vectors  
81 targeting eleven putative tumor suppressors and four control vectors with inert sgRNAs (Lenti-  
82 sgTS<sup>Pool</sup>/Cre; **Fig. 1a**). Tumor suppressors were selected based on common occurrence in human  
83 lung adenocarcinomas and previously suggested roles in oncogenesis<sup>15</sup>. 18 weeks after tumor  
84 initiation, the sgID-BC region from each bulk tumor-bearing lung was PCR amplified and  
85 sequenced to quantify tumor sizes (**Fig. 1a**).

86 We optimized our Tuba-seq experimental protocols and analysis pipeline to eliminate  
87 sgRNA-sgID/barcode uncoupling due to lentiviral template switching and to minimize PCR,  
88 sequencing, and clustering errors (**Fig. 1b**, **Supplementary Fig. 1a**, and **Methods**)<sup>15</sup>. Our new  
89 streamlined pipeline essentially eliminated the impact of read errors, as assessed by multiple  
90 metrics, including the remaining spurious tumors from spike-in barcodes with known sequences  
91 and correspondence of tumor barcodes with those from the lentiviral plasmid pool (**Fig. 1c, d**,  
92 **Supplementary Fig. 1b**). Quantification of the impact of tumor suppressor gene inactivation on  
93 tumor growth in *KT*; *H11*<sup>LSL-Cas9</sup> mice using our optimized method uncovered effects that were  
94 generally consistent with our previous analyses but with greater magnitudes of tumor  
95 suppression (**Fig. 1e**; **Supplementary Fig. 1c, d** and **2**, sign test for differences in magnitudes, *P*  
96 = 0.001)<sup>14</sup>. Consistent with the robustness of our methods, analysis of the *KT* mice with Lenti-  
97 sgTS<sup>Pool</sup>/Cre-initiated tumor revealed no false-positive tumor suppressive effects  
98 (**Supplementary Fig. 1d, e**).

99           When quantifying tumor suppressor gene effects using Tuba-seq, each mouse represents  
100          an internally controlled experiment in which tumor size metrics can be normalized to tumors  
101          with inert sgRNAs within the same animal (**Fig. 1e, Supplementary Fig. 1**)<sup>15</sup>. In contrast,  
102          comparing tumor size distributions among groups of mice, such as between untreated and drug-  
103          treated groups, requires methods that overcome the technical and biological differences between  
104          mice. To address these challenges, we rigorously modeled drug responses and genotype-specific  
105          responses under the assumption that while tumors of all sizes respond equally to each treatment,  
106          the treatment effect can vary by genotype. Specifically, we estimated the drug effect on control  
107          tumors (those with inert sgRNAs) and then applied this effect to all tumors to calculate an  
108          expected distribution of tumor sizes after treatment (**Fig. 2a** and **Methods**). Genotype-specific  
109          therapeutic responses (GSTRs) were quantified by comparing the observed distribution of tumor  
110          sizes for tumors of a certain genotype after treatment with the expected distribution derived from  
111          the untreated mice. We developed two statistics to characterize GSTRs, the first is based on the  
112          relative numbers of tumors above a certain size after treatment (*ScoreRTN* – Relative Tumor  
113          Number) and the second compares the geometric mean of tumors from the full distribution of  
114          tumor sizes (*ScoreRGM* – Relative Geometric Mean) (**Methods**). By assessing the performance  
115          of the two statistics, we showed that both statistics are unbiased and have substantial and similar  
116          power although one statistic may outperform the other if the genotype-specific response is not  
117          uniform across tumor sizes (**Methods, Fig. 2b-c** and **Supplementary Fig. 3, 4** and **5**).

118           We applied Tuba-seq and our statistical metrics to assess the genotype-specific  
119          therapeutic responses of 11 genotypes of lung tumors to a panel of eight single and combination  
120          therapies (**Fig. 1a** and **2d**). These therapies were chosen to perturb diverse signaling pathways  
121          and assess the genotype-dependency of chemotherapy responses. *KT;H1I*<sup>LSL-Cas9</sup> mice with

122 Lenti-sg $TS^{Pool}$ /Cre-initiated lung tumors were treated for three weeks with one of the eight  
123 therapies followed by Tuba-seq analysis (**Fig. 1a**). The total cancer cell numbers estimated by  
124 Tuba-seq were highly correlated with total tumor-bearing lung weights, which varied  
125 substantially among mice even within the same groups (**Supplementary Fig. 6a-c**). Despite such  
126 mouse-to-mouse variation, analysis of the overall tumor burden and the number of tumors with  
127 inert sgRNAs identified significant overall effects of five treatments (**Supplementary Fig. 6**).

128 We compared the tumor size profiles of treated mice with those of untreated mice and  
129 calculated the *ScoreRTN* and *ScoreRGM* (**Supplementary Fig. 7**). For both statistics, we  
130 estimated the magnitudes of GSTR and the associated *P*-values. Across all genotypes and  
131 treatments, the two statistics were well-correlated in magnitude as expected under the model of  
132 proportional tumor responses (**Supplementary Fig. 7b**;  $r = 0.86$ ,  $P=10^{-46}$ ). Among the 88  
133 assessed genotype-treatment pairs, 20 and 17 significant GSTRs ( $P < 0.05$ ) were identified by  
134 *ScoreRTN* and *ScoreRGM*, respectively. Of these, 19 genotype-treatment interactions were  
135 significant by one statistic ( $P < 0.05$ ) and at least marginally significant ( $P < 0.1$ ) by the other  
136 (**Supplementary Fig. 7a, b; Table S1**). We derived a composite measure of GSTR ( $\hat{G}$ ) with the  
137 magnitude estimated from the inverse variance weighted average of the two statistics (**Methods**,  
138 **Fig. 2f**). Analysis of genotype-specific effects across treatments highlighted similarities among  
139 tumor suppressors, including those of Lkb1 and Setd2 known to have redundant tumor  
140 suppressive effects<sup>5</sup>, while combination treatments clustered with their corresponding single  
141 therapies (**Supplementary Fig. 7c, d**). Power analysis showed that our findings were robust to  
142 the choice of inert sgRNAs, cancer cell number cutoff, and inaccurate estimation of drug effect  
143 (**Supplementary Fig. 8, 9**).

144 Only one of the detected GSTRs was known in advance – the resistance of Rb1-deficient  
145 tumors to the CDK4/6 inhibitor, palbociclib. This resistance is consistent with the biochemical  
146 features of this pathway and clinical findings in breast cancer and hepatocellular carcinoma<sup>16-18</sup>  
147 (**Supplementary Fig. 11f**). Our ability to rediscover this interaction serves as a positive control  
148 of our method and is consistent with the expectation that some pharmacogenomic interactions  
149 transcend cancer types.

150 To further test the performance of our experimental and statistical procedures, we  
151 performed two additional experiments. First, as a negative control for GSTR identification, we  
152 treated Cas9-negative *KT* mice with a combination of chemotherapy and Mek-inhibition  
153 (**Supplementary Fig. 10a**). This treatment led to a dramatic reduction in tumor sizes compared  
154 to untreated *KT* mice (**Supplementary Fig. 10b**). Only one false positive GSTR was identified  
155 (*ScoreRTN*,  $P = 0.03$ ; *ScoreRGM*,  $P = 0.07$ ) with a very weak magnitude of the effect ( $\hat{G} = 0.093$ ,  
156 while the minimum magnitude of significant GSTR in the main experiment was 0.108; **Fig. 2g**).  
157 Combined with the fact that none of the individual inert sgRNAs (*sgNeo1*, *sgNeo2*, *sgNeo3*, and  
158 *sgNT*) had significant effects by either metric for any of the treatments in our main  
159 pharmacogenomic mapping experiment, this experiment provided additional confidence in the  
160 veracity of the detected GSTRs (**Fig. 2f, g**).

161 Simulation suggests that these cohort sizes have substantial power (**Supplementary Fig.**  
162 **4**); therefore, we next attempted to rediscover the genotype-palbociclib interactions. We initiated  
163 tumors in a similar, albeit somewhat smaller cohort of *KT;H11<sup>LSL-Cas9</sup>* mice with Lenti-  
164 *sgTS<sup>Pool</sup>/Cre* and repeated the palbociclib-treatment. Analyses of these mice again identified *Rb1*-  
165 inactivation as a mediator of palbociclib resistance (**Fig. 2f, Supplementary Fig. 10**). *Smad4*-  
166 deficient tumors, which showed modest resistance in our initial experiment, showed nominal

167 resistance in the repeat experiment ( $\hat{G} = 0.167$ ), although this interaction was not significant  
168 ( $P=0.17$  and 0.20 for *ScoreRTN* and *ScoreRGM*, respectively).

169 While the positive and negative predictive values of cancer cell line studies are often  
170 questioned<sup>19</sup>, the scale at which these *in vitro* studies can be performed has enabled the  
171 generation of drug response data across large panels of cell lines<sup>4,20</sup>. We compared our findings  
172 to the largest dataset of cell line-therapeutic responses (Genomics of Drug Sensitivity in Cancer;  
173 GDSC)<sup>3</sup> in which all five of our monotherapies were assessed (paclitaxel, palbociclib,  
174 phenformin, everolimus/rapamycin, and trametinib)<sup>3</sup>. Among the genotype-treatment pairs  
175 assessed in both studies, nine had significant effects in our analysis, but only one of these  
176 genotype-treatment interactions was significant in GDSC (*Rb1*-palbociclib)(**Fig. 2i** and  
177 **Supplementary Fig 12**). Three of the significant genotype-specific resistances, which were only  
178 uncovered *in vivo*, involved *Smad4*-deficiency (**Fig. 2i**). Given the absence of microenvironment  
179 stimulation of the TGFβ/Smad4 pathway in culture, these findings suggest that targeting  
180 paracrine TGFβ signaling could reduce the efficacy of cancer therapies in some contexts<sup>21</sup>.

181 Although most of the detected pharmacogenomic interactions we uncovered are novel,  
182 several lines of evidence derived from clinical and preclinical data are consistent with our  
183 observations. For instance, *Lkb1*-inactivation reduced sensitivity to mTOR inhibition in our data,  
184 which is supported by previous anecdotal data from the analysis of lung adenocarcinoma patient-  
185 derived primary cultures *in vitro* (**Supplementary Fig. 13**)<sup>5</sup>. The ultimate goal of our study is to  
186 find genotype-treatment responses that predict lung adenocarcinoma patient responses. Lung  
187 adenocarcinoma patients are often treated with first-line platinum-containing combination  
188 therapies. In our analysis, *Keap1*-inactivation specifically led to resistance to treatments that  
189 included carboplatin, while not promoting significant resistance to the other therapies (**Fig. 2f**).

190 To investigate the clinical impact of tumor suppressor genotype on lung adenocarcinoma  
191 responses, we queried the tumor suppressor genotypes and therapeutic benefit of platinum-  
192 containing treatments (assessed as time-to-next-treatment) of 216 oncogenic *KRAS*-driven  
193 human lung adenocarcinoma patients treated at Memorial Sloan Kettering Cancer Center  
194 (**Methods**). When each gene was assessed individually, both *KEAP1* and *LKB1* mutations were  
195 associated with worse clinical outcomes ( $P=6\times10^{-6}$ , **Fig 2j** and  $P = 0.06$ , **Supplementary Fig.**  
196 **14j**, respectively). However, the marginally significant effect of *LKB1* mutation appears to be  
197 driven by the co-occurrence of *KEAP1* mutations with *LKB1* mutations (**Supplementary Fig.**  
198 **14**). This is also well supported by our pharmacogenomic data in which *Lkb1*-inactivation did  
199 not confer resistance to platinum-containing treatments (**Fig. 2f**). We further quantified the  
200 hazard ratio of the mutational status of the 11 genes in a manner that takes into account the effect  
201 of other co-incident mutations. This analysis confirmed that mutation of *KEAP1* correlated with  
202 a shorter time-to-next-treatment, which is consistent with our Tuba-seq results as well as a  
203 previous study on the impact of *KEAP1/NRF2*-pathway alterations on platinum responses (**Fig.**  
204 **2j, k**)<sup>22,23</sup>. Our *in vivo* pharmacogenomic platform, in which the responses of tumors with  
205 defined genotypes can be quantified, establishes direct causal relationships between genotype  
206 and treatment responses and enables accurate interpretation of patient data.

207 We uncovered a surprisingly complex pharmacogenomic map of resistance and  
208 sensitivity of *KRAS*-driven lung adenocarcinoma. Across diverse tumor suppressor genotypes  
209 and treatments, genotype-treatment interactions were very common (~20% in our study),  
210 suggesting that genetic differences among tumors may underlie much of the heterogeneity in  
211 treatment responses. Our study required only a small number of animals, thus highlighting the  
212 power of our platform in confirming existing, and prioritizing new, genotype-specific drug

213 responses (**Supplementary Fig. 15**). The exploitation of this platform to quantify the effects of  
214 additional therapies (and combination therapies) across a greater diversity of cancer genotypes  
215 will provide a cause-and-effect pharmacogenomic framework from which novel biological  
216 hypotheses and precision treatment approaches will emerge.

217

218 **References:**

- 219 1 Roychowdhury, S. & Chinnaiyan, A. M. Translating genomics for precision cancer  
220 medicine. *Annu Rev Genomics Hum Genet* **15**, 395-415, doi:10.1146/annurev-genom-  
221 090413-025552 (2014).
- 222 2 van de Haar, J. *et al.* Identifying Epistasis in Cancer Genomes: A Delicate Affair. *Cell* **177**,  
223 1375-1383 (2019).
- 224 3 Iorio, F. *et al.* A Landscape of Pharmacogenomic Interactions in Cancer. *Cell* **166**, 740-  
225 754, doi:10.1016/j.cell.2016.06.017 (2016).
- 226 4 Barretina, J. *et al.* The Cancer Cell Line Encyclopedia enables predictive modelling of  
227 anticancer drug sensitivity. *Nature* **483**, 603-607, doi:10.1038/nature11003 (2012).
- 228 5 Lee, J. K. *et al.* Pharmacogenomic landscape of patient-derived tumor cells informs  
229 precision oncology therapy. *Nat Genet* **50**, 1399-1411, doi:10.1038/s41588-018-0209-6  
230 (2018).
- 231 6 Roper, N., Stensland, K. D., Hendricks, R. & Galsky, M. D. The landscape of precision  
232 cancer medicine clinical trials in the United States. *Cancer Treat Rev* **41**, 385-390,  
233 doi:10.1016/j.ctrv.2015.02.009 (2015).
- 234 7 Hidalgo, M. *et al.* Patient-Derived Xenograft Models: An Emerging Platform for  
235 Translational Cancer Research. *Cancer discovery* **4**, 998-1013, doi:10.1158/2159-  
236 8290.CD-14-0001 (2014).
- 237 8 Ben-David, U. *et al.* Patient-derived xenografts undergo mouse-specific tumor evolution.  
238 *Nat Genet* **49**, 1567-1575, doi:10.1038/ng.3967 (2017).
- 239 9 Hoffman, R. M. J. N. R. C. Patient-derived orthotopic xenografts: better mimic of  
240 metastasis than subcutaneous xenografts. **15**, 451 (2015).
- 241 10 Gao, H. *et al.* High-throughput screening using patient-derived tumor xenografts to  
242 predict clinical trial drug response. **21**, 1318 (2015).
- 243 11 Kersten, K., de Visser, K. E., van Miltenburg, M. H. & Jonkers, J. Genetically engineered  
244 mouse models in oncology research and cancer medicine. *EMBO Mol Med* **9**, 137-153,  
245 doi:10.15252/emmm.201606857 (2017).
- 246 12 Singh, M., Murriel, C. L. & Johnson, L. J. C. r. Genetically engineered mouse models:  
247 closing the gap between preclinical data and trial outcomes. **72**, 2695-2700 (2012).
- 248 13 Chen, Z. *et al.* A murine lung cancer co-clinical trial identifies genetic modifiers of  
249 therapeutic response. *Nature* **483**, 613-617, doi:10.1038/nature10937 (2012).

- 250 14 Rogers, Z. N. *et al.* Mapping the in vivo fitness landscape of lung adenocarcinoma tumor  
251 suppression in mice. *Nat Genet* **50**, 483-486, doi:10.1038/s41588-018-0083-2 (2018).
- 252 15 Rogers, Z. N. *et al.* A quantitative and multiplexed approach to uncover the fitness  
253 landscape of tumor suppression in vivo. *Nat Methods* **14**, 737-742,  
254 doi:10.1038/nmeth.4297 (2017).
- 255 16 Bolland, J. *et al.* Palbociclib (PD-0332991), a selective CDK4/6 inhibitor, restricts tumour  
256 growth in preclinical models of hepatocellular carcinoma. *Gut* **66**, 1286-1296,  
257 doi:10.1136/gutjnl-2016-312268 (2017).
- 258 17 Knudsen, E. S., Pruitt, S. C., Hershberger, P. A., Witkiewicz, A. K. & Goodrich, D. W. Cell  
259 Cycle and Beyond: Exploiting New RB1 Controlled Mechanisms for Cancer Therapy.  
260 *Trends Cancer* **5**, 308-324, doi:10.1016/j.trecan.2019.03.005 (2019).
- 261 18 O'Leary, B. *et al.* The Genetic Landscape and Clonal Evolution of Breast Cancer  
262 Resistance to Palbociclib plus Fulvestrant in the PALOMA-3 Trial. *Cancer discovery* **8**,  
263 1390-1403, doi:10.1158/2159-8290.CD-18-0264 (2018).
- 264 19 Haibe-Kains, B. *et al.* Inconsistency in large pharmacogenomic studies. *Nature* **504**, 389-  
265 393, doi:10.1038/nature12831 (2013).
- 266 20 Garnett, M. J. *et al.* Systematic identification of genomic markers of drug sensitivity in  
267 cancer cells. *Nature* **483**, 570-575, doi:10.1038/nature11005 (2012).
- 268 21 Papageorgis, P. & Stylianopoulos, T. Role of TGFbeta in regulation of the tumor  
269 microenvironment and drug delivery (review). *Int J Oncol* **46**, 933-943,  
270 doi:10.3892/ijo.2015.2816 (2015).
- 271 22 Jeong, Y. *et al.* Role of KEAP1/NFE2L2 Mutations in the Chemotherapeutic Response of  
272 Patients with Non-Small Cell Lung Cancer. *Clin Cancer Res*, doi:10.1158/1078-0432.CCR-  
273 19-1237 (2019).
- 274 23 Arbour, K. C. *et al.* Effects of Co-occurring Genomic Alterations on Outcomes in Patients  
275 with KRAS-Mutant Non-Small Cell Lung Cancer. *Clin Cancer Res* **24**, 334-340,  
276 doi:10.1158/1078-0432.CCR-17-1841 (2018).
- 277 24 Jackson, E. L. *et al.* Analysis of lung tumor initiation and progression using conditional  
278 expression of oncogenic K-ras. *JNCI* **15**, 3243-3248 (2001).
- 279 25 Chiou, S. H. *et al.* Pancreatic cancer modeling using retrograde viral vector delivery and  
280 in vivo CRISPR/Cas9-mediated somatic genome editing. *Genes Dev* **29**, 1576-1585,  
281 doi:10.1101/gad.264861.115 (2015).
- 282 26 Madisen, L. *et al.* A robust and high-throughput Cre reporting and characterization  
283 system for the whole mouse brain. *Nat Neurosci* **13**, 133-140, doi:10.1038/nn.2467  
284 (2010).
- 285 27 MacConaill, L. E. *et al.* Unique, dual-indexed sequencing adapters with UMIs effectively  
286 eliminate index cross-talk and significantly improve sensitivity of massively parallel  
287 sequencing. *BMC Genomics* **19**, 30, doi:10.1186/s12864-017-4428-5 (2018).
- 288 28 Pezza, J. A., Kucera, R. & Sun, L. J. N. E. B. Polymerase fidelity: what is it, and what does  
289 it mean for your PCR. (2014).
- 290 29 Sinha, R. *et al.* Index switching causes “spreading-of-signal” among multiplexed samples  
291 in Illumina HiSeq 4000 DNA sequencing. 125724 (2017).

- 292 30 Murray, C. W. *et al.* An LKB1-SIK Axis Suppresses Lung Tumor Growth and Controls  
293 Differentiation. *Cancer discovery* **9**, 1590-1605, doi:10.1158/2159-8290.CD-18-1237  
294 (2019).
- 295 31 Cheng, D. T. *et al.* Memorial Sloan Kettering-Integrated Mutation Profiling of Actionable  
296 Cancer Targets (MSK-IMPACT): A Hybridization Capture-Based Next-Generation  
297 Sequencing Clinical Assay for Solid Tumor Molecular Oncology. *J Mol Diagn* **17**, 251-264,  
298 doi:10.1016/j.jmoldx.2014.12.006 (2015).
- 299

300

301

302 **Acknowledgements:**

303 We thank the Laura Andrejka for technical support; A. Orantes for administrative support;  
304 member of the Stanford Animal care staff for excellent animal care; D. Feldser, J. Sage, J.  
305 Zhang, and members of the Winslow and Petrov laboratories for helpful comments. C.L. is the  
306 Connie and Bob Lurie Fellow of the Damon Runyon Cancer Research Foundation (DRG-2331).  
307 W-Y.L. was supported by an American Association of Cancer Research Postdoctoral fellowship  
308 (17-40-18-LIN). H.R. was supported by the Druckenmiller Center for Lung Cancer Research at  
309 MSK. H.C. was supported by a Tobacco-Related Disease Research Program Postdoctoral  
310 Fellowship (28FT-0019). C.D.M was supported by NIH K99-CA226506. M.Y. was supported  
311 by a Stanford Dean's fellowship, an American Lung Association senior research training grant,  
312 and NIH F32-CA236311. I.P.W was supported by the NSF Graduate Research Fellowship  
313 Program and NIH F31-CA210627. This work was supported by NIH R01-CA207133 (to  
314 M.M.W and D.A.P.), NIH R01-CA231253 (to M.M.W and D.A.P), NIH R01-CA234349 (to  
315 M.M.W and D.A.P.) and Memorial Sloan Kettering Cancer Center Support Grant/Core Grant  
316 (P30 CA008748).

317

318 **AUTHOR CONTRIBUTIONS**

319 C.L., W.L., M.M.W., D.A.P., and C.M.R. planned the project. C.L. performed bioinformatics  
320 and statistical analysis. W.L., H.C., M.M.W., Z.R., and M.Y. performed the mice experiment.  
321 H.R. collected the patient response dataset. H.R. and C.L. performed the analysis on human  
322 dataset. Z.N.R., I.P.W., and C.D.M. assisted in the mice experiments. C.L., M.M.W and D.A.P.  
323 wrote the paper.

324

325

326

327 **COMPETING INTERESTS**

328 D.A.P., I.P.W, and M.M.W are cofounders of D2G Oncology Inc. D.A.P., I.P.W, Z.N.R, C.D.M  
329 and M.M.W hold equity in D2G Oncology Inc.

330

331

332

333

334

335

336

337

338

339

340

341 **MATERIALS AND METHODS**

342 **Generation of lentiviral vectors**

343 The design and barcoding of Lentiviral sgRNA/Cre vectors were previously described<sup>15</sup>.  
344 Briefly, each vector contains a guide RNA (sgRNA) targeting a specific tumor suppressor gene,  
345 a highly diverse barcode region (BC) (total length 23 bp, the length of the diverse sequence is  
346 15bp), and an sgID sequence of 8 bp that is specific to each sgRNA. The BC and sgID regions  
347 are adjacent to one another and can be amplified in a single PCR reaction. To eliminate sgID-  
348 BC-sgRNA uncoupling driven by lentiviral template switching during reverse transcription of  
349 the pseudo-diploid viral genome, we produced each barcoded Lenti-sgRNA/Cre vector  
350 separately. We transfected 293T cells with individual barcoded Lenti-sgRNA/Cre plasmids  
351 (*sgApc*, *sgAtm*, *sgArid1a*, *sgCdkn2a*, *sgKeap1*, *sgLkb*, *sgNeo1*, *sgNeo2*, *sgNeo3*, *sgNT1*, *sgp53*,  
352 *sgRb1*, *sgRbm10*, *sgSetd2*, and *sgSmad4*) and packaging plasmids (delta8.2 and VSV-G) using  
353 polyethylenimine-based transfection. The supernatant was collected at 48 and 72 hours after  
354 transfection. Each lentiviral vector was filtered and concentrated by ultracentrifugation (25,000g  
355 for 1.5 hours), resuspended in PBS, and frozen in aliquots at -80°C. To determine the titer of each  
356 vector, we transduced LSL-YFP cells (a gift from Dr. Alejandro Sweet-Cordero/UCSF),  
357 determined the percent YFP-positive cells by flow cytometry, and calculated the titer by  
358 comparing to a lentiviral preparation of a known titer. Viral vectors were thawed and pooled  
359 immediately prior to delivery to mice.

360 **Mice, tumor initiation, and drug treatment**

361 *Kras*<sup>LSL-G12D</sup> (K), *R26*<sup>LSL-Tomato</sup> (T), *H11*<sup>LSL-Cas9</sup> mice (hereafter *KT;H11*<sup>LSL-Cas9</sup> mice) have  
362 been previously described<sup>24-26</sup>. Lung tumors were initiated using a pool of barcoded Lentiviral-

363 sgRNA/Cre vectors delivered by intratracheal transduction of mice as previously described<sup>15</sup>.  
364 1.1 x 10<sup>5</sup> and 2.2 x 10<sup>4</sup> infectious particles in 60 µl of PBS were administered to each *KT* and  
365 *KT;H11<sup>LSL-Cas9</sup>* mouse, respectively. Tumor burden was assessed by fluorescence microscopy,  
366 lung weight measurement, and histology. Drug treatments were started 15 weeks after tumor  
367 initiation.

368 In the main pharmacogenomic mapping experiment, mice were assigned to eight  
369 treatment arms or 8 mice were left untreated for 3 weeks. There were five arms of  
370 monotherapies. 6 mice were treated with 100 mg/kg palbociclib daily by oral gavage; 5 mice  
371 were treated with 10 mg/kg everolimus daily by oral gavage, 6 mice were treated with 100  
372 mg/kg phenformin daily by oral gavage, 5 mice were treated with 20 mg/kg paclitaxel every  
373 other day by intraperitoneal injection, and 7 mice were treated with 0.3 mg/kg trametinib daily  
374 by oral gavage. For mice treated with drug combinations, the dosing was the same as when each  
375 drug was used for monotherapies. 8 mice were treated with the combination of 20 mg/kg  
376 paclitaxel every other day by intraperitoneal injection and 0.3 mg/kg trametinib daily by oral  
377 gavage; 7 mice were treated with 50 mg/kg carboplatin every 5 days by intraperitoneal injection  
378 in combination with 20 mg/kg paclitaxel every other day by intraperitoneal injection; and 6 mice  
379 were treated by a combination of three drugs: 50 mg/kg carboplatin every 5 days by  
380 intraperitoneal injection, 20 mg/kg paclitaxel every other day by intraperitoneal injection, 0.3  
381 mg/kg trametinib daily by oral gavage.

382 For the palbociclib repeat experiment, 5 mice were left untreated and 5 mice were treated  
383 with 100 mg/kg palbociclib daily by oral gavage. For the negative control experiment, 4 *KT* mice  
384 were left untreated, and 5 *KT* mice were treated with a combination of carboplatin, paclitaxel,  
385 and trametinib with the same dosing as the main experiment, except that treatment was continued

386 for 6 weeks. All mice in all experiments were transduced with the same pool of viral vectors. All  
387 experiments were performed in accordance with Stanford University Institutional Animal Care  
388 and Use Committee guidelines.

389 **Isolation of genomic DNA from mouse lungs, preparation of sgID-BC libraries, and**  
390 **quantification of tumor size**

391 Genomic DNA was isolated from bulk tumor-bearing lung tissue from each mouse as  
392 previously described<sup>15</sup>. Three benchmark “spike-in” cell lines were added to each sample prior  
393 to lysis and DNA-extraction. Spike-in cell lines harbor integrated barcoded Lenti-Cre vectors  
394 with the sgID “TTCTGCCT”, which is distinct from all sgIDs in the Lenti-sgRNA/Cre pool. A  
395 pool of three Spike-in cell lines was added to each bulk lung sample at a known cell number  
396 (~5x10<sup>5</sup> cells per cell line), thus enabling the calculation of the absolute cancer cell number  
397 within each tumor<sup>14</sup>. To determine the absolute number of cancer cells in each tumor, we  
398 multiplied the number of reads of each tumor sgID-BC by the mean number of reads of the three  
399 spike-in cell lines divided by the expected number of cells for each spike-in (5x10<sup>5</sup> cells).

400 Libraries were prepared by PCR amplification of the sgID-BC region from 32 µg of  
401 genomic DNA per mouse. To enable the identification and subsequent computational elimination  
402 of possible index-hopped reads in high-throughput sequencing, the sgID-BC region of the  
403 integrated Lenti-sgRNA-BC/Cre vectors was PCR amplified from each sample with unique dual  
404 indexed primer pairs<sup>27</sup>. Because Illumina short-read sequencing platforms require high library  
405 sequence diversity for accurate base calls, we previously added 50% PhiX phage DNA to each  
406 amplicon library before sequencing as recommended by Illumina. To further improve sequencing  
407 quality and minimize the use of PhiX DNA, we improved our previous method by adding 6 to 9  
408 random nucleotides (Ns) to the flanking ends of both index primers before the sequence-specific

409 primers. These random bases increase sequence diversity through their high nucleotide diversity  
410 and by desynchronizing the barcode regions of the amplicon library (via differing 6-9 nucleotide  
411 offsets). This reduced the needed PhiX genomic DNA from 50% to 10% and greatly improved  
412 Q30 scores.

413 Forward primers were of the form:

414 5'- AATGATACGGCGACCACCGAGATCTACAC**A**GCGCTAG

415 *ACACTCTTCCCTACACGACGCTTTCCGATCT [N]<sub>6-9</sub>GCGCACGTCTGCCGCGCTG* -3'

416

417 Reverse primers were of the form:

418 5'- CAAGCAGAAGACGGCATACGAGAT**C**GTGAT

419 *GTGACTGGACTTCAGACGTGTGCTTTCCGATCT [N]<sub>6-9</sub>CAGGTTCTGCGAACCTCAT* -3'

420 The underlined sequences denote regions that bind the template; the bolded sequences are  
421 the dual indexes which are unique to each mouse library pooled on the same sequencing lane; the  
422 italicized regions are the Illumina® TruSeq Universal adapter sequence, and the sequences 5' of  
423 the Indexes are the P5 and P7 adaptors.

424 We used a single-step PCR amplification of sgID-BC regions. We performed eight 100  
425 μl PCR reactions per sample (4 μg DNA per reaction) using Q5 High-Fidelity 2x Master Mix  
426 (New England Biolabs)<sup>28</sup> to maximize library sequencing quality. Pooled PCR products were  
427 isolated by gel electrophoresis and gel extracted using the Qiagen® MinElute Gel Extraction kit.  
428 The concentration of purified PCR products from each sample was determined by Bioanalyzer  
429 (Agilent Technologies) and pooled for sequencing. Pooled libraries were cleaned up and size-  
430 selected using AMPure XP beads (Beckman Coulter). Libraries were sequenced on an Illumina®  
431 HiSeq 2500 to generate paired-end 150 bp reads. Unlike patterned flow cells (e.g., HiSeq 4000),

432 nonpatterned flow cells used by HiSeq 2500 exhibit extremely low index hopping rates<sup>29</sup>. Paired-  
433 end sequencing was used to ensure the fidelity of our barcode calls.

434 **Processing reads to identify the sgID and barcode**

435 By systematically improving DNA library preparation and sequencing, we dramatically  
436 improved the quality of our barcoded tumor calls. In doing so, our previous DADA2-based  
437 denoising approach became obsolete, and a new, more stringent computational analysis pipeline  
438 that completely eliminated spurious tumors from PCR and sequencing errors was developed.

439 Read sequences are expected to contain an 8-nucleotide sgID region followed by a 23-  
440 nucleotide BC (AANNNNNTTNNNNNAANNNN). We required both the forward and reverse  
441 sequencing reads to match perfectly within the BC region. This stringent requirement minimizes  
442 sequencing errors that will generate sgID-BC reads that do not represent actual clonal tumors  
443 within the samples. The FASTQ files of each technical replicate were combined for all analyses  
444 except when used for evaluating the reproducibility and quantifying error.

445 FASTQ files were processed to identify the sgID and BC counts for each tumor. The  
446 sgID region identified the targeted tumor suppressor gene, which we identified from the forward  
447 read alone, again allowing no mismatches or indels relative to the expected sgID sequences. Note  
448 that all sgID sequences differ by at least 2 nucleotides from each other, making this step robust to  
449 sequencing errors. The number of reads with each unique sgID-BC in each sample were added  
450 up to arrive at the size of each putative tumor (in the units of the number of reads).

451     **Identification of unique tumors from random barcodes and removal of “spurious tumor”**  
452     **generated by read errors**

453                 PCR and sequencing errors within the random barcode regions may be misinterpreted as  
454     unique tumors. These spurious tumors bias the analysis of tumor size distribution, reduce signals  
455     of tumor suppression, and potentially confound our ability to detect GSTR using Tuba-seq.  
456     Therefore, we used stringent criteria to reduce and even eliminate the effects of PCR and  
457     sequencing errors on tumor calls.

458                 The random barcode in the sgID-BC region is 15 nucleotides long. Thus, there is a  
459     theoretical potential diversity of  $\sim 4^{15} > 10^9$  barcodes within each lentiviral vector. While the  
460     actual diversity in each Lenti-sgRNA/Cre vector is dictated by the number of colonies generated  
461     during the plasmid barcoding step, this theoretical diversity guarantees that any two genuine  
462     tumors will be very unlikely to have barcodes within a certain Hamming distance from one  
463     another. Only approximately one pair of true tumors is expected to have barcodes that are only  
464     two nucleotides different from each other when making all pair-wise comparison in a set of 1000  
465     tumors. Thus, we expect that most reads within two nucleotides from each other within the same  
466     mouse library are most likely due to sequencing/PCR errors. Therefore, we designed a pipeline  
467     in which any “tumor” with a barcode that was within a Hamming distance of two from a larger  
468     tumor in the same sample was excluded from subsequent analysis. As anticipated, excluded  
469     tumors were greatly enriched at the lowest end of the tumor size distribution, and were most  
470     often orders of magnitude smaller than the larger tumor with a similar barcode (Mann-Whitney  
471     U test of tumor sizes in the comparison between the removed and the remaining tumors,  $P < 10^{-300}$ ).  
472     Thus, we elected to remove such putatively spurious tumors from subsequent analysis.  
473     Previously, we combined the smaller “spurious” tumors into the larger tumor with the similar

474 barcode, as PCR and sequencing errors were more common and constituted a non-negligible  
475 fraction of the sequenced library. However, with our improved approach, these spurious tumors  
476 constituted only ~ 0.3% of all reads and are necessarily more likely to be distinct tumors (as  
477 spurious tumors are now rarer), so we did not merge spurious tumors into their larger partners in  
478 this analysis. Because of the very small quantity of spurious tumors in our new approach, the  
479 decision to merge (or not merge) tumors have negligible effects on tumor size estimates.

480 To determine whether our stringent filtering removed most spurious tumors, we first  
481 estimated a False Positive Rate using our spike-in cell lines. We assessed whether any spurious  
482 tumors were generated from our spike-in controls for which we know the exact sequence of the  
483 sgID-BC. In these spike-ins, any sgID-BC read (i.e., with the spike-in sgID) containing a BC  
484 sequence that differs from the three known correct BCs is presumably generated by PCR or  
485 sequencing errors. Hence, these anomalous spike-in barcodes can be used to estimate the  
486 occurrence of spurious tumors. Before applying our filtering pipeline, we detected many such  
487 spurious barcode reads – 843 spurious spike-in “tumors” in a typical sequencing lane (**Fig. 1c**).  
488 Our new stringent filtering removed all of them.

489 We next identified true positive tumors by sequencing the sgID-BC region in each  
490 plasmid pool used to generate the lentiviral vectors in the Lenti-sgTS<sup>Pool</sup>/Cre pool. Given the  
491 tremendous theoretical diversity of our random barcodes, barcodes detected in *both* the plasmid  
492 pool and the mouse lungs are very likely to be genuine. We used these data to assess the  
493 presence of spurious tumors in the mouse lung as these should almost never be detected in the  
494 plasmid pool. However, a false positive rate cannot be directly measured from this plasmid  
495 sequencing data because barcode diversity in the plasmid pool is too high to be exhaustively  
496 sequenced to cover every potential barcode, i.e., not all barcodes present in the plasmid pool

497 were captured in the barcodes sequenced from the plasmids. Thus, some genuine tumors in the  
498 mice will have barcodes not captured in the plasmid sequencing. Nevertheless, in a well-  
499 calibrated analysis pipeline, the rate at which genuine tumors are detected should not vary with  
500 tumor size. We determined whether the smaller tumors – which are more likely to be polluted by  
501 spurious tumors – exhibit a lower probability of detection in the plasmid pool. Before the  
502 application of our filtering procedure, 92.1% of tumors larger than 1000 cells, but only 87.9% of  
503 tumors smaller than 1000 cells were detected in the plasmid pool (Chi-squared test,  $p < 10^{-300}$ ).  
504 This decline in the true positive tumor fraction with tumor size suggests that some spurious small  
505 tumors exist in our data prior to filtering. However, after our filtering procedure, 92.7% of  
506 tumors larger than 1000 cells and 93.1% of tumors smaller than 1000 cells were detected in the  
507 plasmid pool (**Fig. 1d** and **Supplementary Fig. 1b**). This consistency of the true tumor rate  
508 across tumor size suggests that filtering effectively eliminated spurious tumors. Along with our  
509 analysis of spurious spike-ins, both results suggest that our filtering procedure effectively  
510 eliminates spurious tumors.

511 **Summary statistics for characterizing tumor growth**

512 Because GSTR can manifest as a mean effect or a change in the shape of tumor size  
513 distributions, we used a variety of summary statistics to characterize tumor growth, including  
514 percentiles, Log-normal (LN) mean, geometric mean, and relative tumor burden. Percentiles and  
515 LN mean were calculated as previously described<sup>15</sup>. Briefly, percentiles are nonparametric  
516 summaries for the distribution. 95<sup>th</sup> percentile for *sgTS* tumors, for instance, is calculated as the  
517 size above which we find the top 5% of the largest *sgTS* tumors and then dividing it by the  
518 corresponding number for the tumors with inert sgRNAs (Inert tumors). The resulting number is  
519 dimensionless. The LN mean is the maximum likelihood estimator of the mean number of

520 neoplastic cells given a log-normal distribution of tumor sizes. The LN mean of sgTS tumors is  
521 relative to the LN mean of the Inert tumors. The geometric mean is defined as the product of all  
522 tumor sizes raised to the inverse of the number of tumors. For calculation, we compute the  
523 arithmetic mean of the logarithm-transformed values of tumor sizes and then use the  
524 exponentiation to return the computation to the original scale. The geometric mean is  
525 proportional to the average growth rate of tumors. Relative tumor burden is calculated as

$$\frac{\sum \text{Neoplastic cell number with the sgID in KTCas9 mice}}{\sum \text{Neoplastic cell number in Inert tumors in KTCas9 mice}} / \frac{\sum \text{Neoplastic cell number with the sgID in KT mice}}{\sum \text{Neoplastic cell number in Inert tumors in KT mice}}$$

527 **Developing unbiased procedures for the detection of genotype-specific drug effects**

528 Previous Tuba-seq analyses focused on comparing the sizes of tumors of different  
529 genotypes within individual mice<sup>14,30</sup>. Such analyses are largely robust to multiple sources of  
530 variation among mice such as (1) variation in the efficiency of viral delivery and the resulting  
531 differences in tumor number and total tumor burden across mice and (2) variation in the library  
532 sequencing depth (each sgID within a mouse is part of the same DNA library reaction).  
533 However, in the current analysis of genotype-specific drug response, we needed to compare  
534 tumor sizes between the two groups of mice – the untreated and the treated – rather than only  
535 comparing the relative behaviors of tumors of different genotypes within mice and then  
536 aggregating the signals across mice. Thankfully, our multiplexed pool of tumor genotypes still  
537 allows us to account for variations among mice, as these effects are still common to all imparted  
538 genotypes. First, however, we must generate a genotype-nonspecific null model of response.  
539 Note that because we used the same viral pool to initiate tumors in all treated and untreated mice,  
540 the initial relative representation of transduced epithelial cells containing each Lenti-sgRNA/Cre  
541 is constant and does not vary across mice. Nevertheless, our null model does not assume that the

542 total numbers of initiated tumors among mice are invariant; only the *proportions* of initiated  
543 tumors with different sgRNAs (sgIDs) remain constant.

544 **Null model of tumor responses with no genotype-specificity**

545 We assume that the therapy affects all tumors proportionally to their sizes (proportional  
546 size reduction) such that the size of each tumor changes from  $X$  to  $X_1 = X \times S$  after the drug  
547 treatment, where  $S$  is the proportion of remaining cancer cells. In other words, we assume that  
548 the therapy kills individual cancer cells with a probability  $1-S$  that is independent of the tumor  
549 size. Under the null model ( $H_0$ ) of no genotype-specific drug responses,  $S$  is constant and does  
550 not depend on the genotype of the tumor. Under the alternative model  $H_1$ ,  $S$  varies depending on  
551 the genotype:  $S_{\text{sgID}, j} = S_{\text{Inert}} \times (1+G_j)$ , with  $G_j$  representing the Genotype Specific Therapeutic  
552 Response (GSTR) of tumors generated by viruses with the specified sgID to the drug  $j$ . If  $G_j > 0$ ,  
553 the inactivation of the tumor suppressor associated with that sgID confers relative resistance; if  
554  $G_j < 0$ , the inactivation of the tumor suppressor associated with that sgID confers relative  
555 sensitivity.

556 **Selection of a size cutoff in untreated mice**

557 To consider how tumor size distributions shift between the null and alternative models,  
558 we must first choose the range of the tumor size distribution to consider. In general, we want to  
559 consider tumors that are large enough to be consistently detected regardless of the sequencing  
560 depth and PCR efficiency in both treated and untreated mice, while using as many tumors as  
561 possible to maximize the statistical power. As shown below, the most extreme treatment reduced  
562 tumor sizes by ~87% ( $S=0.13$ , **Supplementary Fig. 6d**). While the depth of sequencing varies  
563 across mice and treatments, we want to reliably identify tumors in each treated and untreated

564 mouse. The most effective treatment group has the smallest tumors after treatment, for which  
565 the depth of sequencing was ~10 cells/read. Thus, we chose to use the cutoff of  $L = 1000$  cells in  
566 the untreated mice, as tumors will not shrink below 100 cells or 10 reads in all treated mice,  
567 allowing reliable detection and accurate size estimates of tumors in each mouse. **Supplementary**  
568 **Fig. 8** shows that our results are robust to shifting the cutoff to 500 or 1500 cells.

569 **Calculation of proportional size-reduction as the drug effect**

570 We first find the value of the tumor reduction factor  $S$  that leads to the best match  
571 between the distributions of Inert tumors between the treated and untreated group under our  
572 model of proportional tumor reduction. We take the following steps to calculate  $S$ . For each  
573 possible value of  $S$  between 0 (tumors are completely eliminated) and 2 (tumors doubled in size  
574 after treatment), we reduce the sizes of each tumor in the untreated group by  $S$  and calculate the  
575 number of such “shrunk” tumors whose sizes remain above or equal to 1000 cells. We then find  
576 the value of  $S$  such that the median number of such shrunk tumors across all the untreated mice is  
577 closest to the median of the number of observed tumors with the size above or equal to 1000  
578 cells across all the mice in the treated group. Specifically, we use the binary search algorithm to  
579 determine the  $S$  that minimizes the difference between the median numbers of tumors of the  
580 treated and untreated groups. We choose to find the  $S$  that matches the median number of tumors,  
581 rather than the mean across the two groups, as the median is not affected by the outlier mice with  
582 very low or very high numbers of tumors. Since we have prior knowledge that drugs will not  
583 increase overall tumor size, an estimated  $S$  larger than 1 is probably due to mouse-to-mouse  
584 variations. Thus we set  $S$  to 1 when it was estimated to be larger than 1. In **Supplementary Fig.**  
585 **9**, we showed that our estimation is robust to the inaccurate estimation of  $S$ , and the power will  
586 only be reduced slightly when  $S$  was not accurately estimated.

587

588 **Approach 1: Relative tumor number (*ScoreRTN*)**

589 Our first approach defines response as the number of tumors that exceed a minimum size  
590 threshold. The intuition is that, given a known tumor reduction factor  $S$  of the drug, the null  
591 hypothesis for each genotype is that the number of tumors above the cutoff  $L$  in the untreated  
592 mice should match the number above the new cutoff  $L \times S$  in the treated mice. If a GSTR exists  
593 (the alternative model), then the tumors with a specific sgID (*i.e.*, tumors with a particular tumor  
594 suppressor inactivated) are more resistant to the drug than the Inert tumors and more of such  
595 tumors should remain above the adjusted cutoff of  $L \times S$  than expected, while if they are more  
596 sensitive, then fewer of such tumors should remain above the adjusted cutoff of  $L \times S$  – rejecting  
597 the null hypothesis in either case.

598 To test this null hypothesis, we first calculate the ratio of the number of tumors above the  
599 cutoff  $L$  in the untreated mice of a particular sgID to that of the Inert tumors ( $RTN_{i,j,L}$ ),  
600

$$601 RTN_{i,j=untreated,L} = \frac{\sum_k C_{i,j=untreated,k}}{\sum_k C_{Inert,j=untreated,k}}$$

602 *for all mice k and all tumors equal or larger than L*

603 where  $C_{i,j,k}$  is the total number of tumors observed in mouse  $k$  in treatment group  $j$  ( $j$  = untreated  
604 here) carrying sgID  $i$  above the cutoff  $L$ . We then calculate the similar ratio for the treated mice  
605 with a modified cutoff  $L \times S$ ,

$$606 RTN_{i,j,L \times S} = \frac{\sum_k C_{i,j,k}}{\sum_k C_{Inert,j,k}} \text{ *for all mice k and all tumors larger than } L \times S\text{}}*$$

607 The null hypothesis can then be expressed as the expectation that

608                    $RTN_{i,untreated,L} = RTN_{i,j,L \times S}$

609     or alternatively that:

610                    $ScoreRTN_{i,j} = \log_2 \left( \frac{RTN_{i,j,L \times S}}{RTN_{i,Untreated,L}} \right) = 0$

611     Under the alternative hypothesis where  $ScoreRTN_{i,j} \neq 0$ , a positive sign of  $ScoreRTN_{i,j}$   
612     suggests that the tumors with a particular sgID are more resistant than the Inert tumors, while a  
613     negative sign suggests the tumors are more sensitive than Inert tumors.

614                 Although directly comparing the size or number of tumors above a constant cutoff  
615     (e.g., 1000 cells), for both the untreated and treated groups may seem intuitive and simpler, such  
616     a comparison generates complex expectations of tumor number that depend both on the  
617     distributions of tumor sizes prior to treatment and the magnitude of the drug effect  
618     (**Supplementary Fig. 3**).

619

620     **Approach 2: Relative geometric mean ( $ScoreRGM$ )**

621                 The second metric,  $ScoreRGM$ , compares the geometric mean of tumors carrying sgID  $i$   
622     relative to the Inert tumors in the untreated and treated groups. The intuition is that if we analyze  
623     a comparable number of tumors in the untreated and treated mice when there is no  $GSTR$ , the  
624     relative growth advantage of tumors carrying a specific sgID (sgID  $i$ ) relative to Inert tumors,  
625     represented by the relative geometric mean, will remain constant. Under the alternative model, if  
626     the tumors with a specific sgID (sgID  $i$ ) are more resistant to the drug than the Inert tumors, then  
627     the relative geometric mean for sgID  $i$  will be larger in the treated group, while if they are more  
628     sensitive, then the relative geometric mean for sgID  $i$  will be smaller. While  $RTN$  does not use  
629     the numeric value of tumor size other than comparing it with the cutoff, (*i.e.*, a tumor with size

630 1001 cells and a tumor with size  $10^7$  cells are both counted as a single tumor above the cutoff of  
631 1000 cells), *RGM* incorporates such tumor size profile information. Hence, *RGM* and *RTN* are  
632 not entirely redundant as they incorporate different information about *GSTR*. Based on power  
633 analysis, *ScoreRTN* is a more sensitive metric in detecting *GSTRs* (**Fig 2b, c**, and  
634 **Supplementary Fig. 4**), particularly when only smaller tumors show *GSTR* (**Supplementary**  
635 **Fig. 5a**). However, when only larger tumors show *GSTR*, the *ScoreRGM* is more likely to  
636 capture it, as large tumors are unlikely to fall below the given size threshold. For instance, in an  
637 extreme case, when only large tumors with over 4000 cells show resistance, *ScoreRTN* will fail  
638 to capture the signals that *ScoreRGM* identifies with reasonable power (**Supplementary Fig.**  
639 **5b**).

640 We denote the total tumor count ( $T$ ) with a certain sgRNA ( $i$ ) in an individual mouse ( $k$ )  
641 in the treated group ( $j$ ) as  $T_{i,j,k}$ . Here, we do not limit tumors to those above 1000 cells but rather  
642 count any tumor with greater than or equal to 2 reads (after the stringent filtering described  
643 above) as a tumor. For an untreated mouse, the proportion of initiated tumors of each sgID can  
644 be approximated by  $R_i$ , the ratio of  $T_{i,untreated,k}$  to  $T_{Inert,untreated,k}$ :

$$645 R_i = \text{median}\left(\frac{T_{i,untreated,k}}{T_{Inert,untreated,k}} \mid \text{for all mice } k\right)$$

646 We then take the top  $N$  tumors with sgRNA  $i$  from mouse  $k$  treated by drug  $j$  as:

$$647 N_{i,j,k} = C_{i,j,k} \times R_i$$

648 where  $C_{i,j,k}$  is the total number of Inert tumors observed in each mouse above the cutoff  $L \times S$   
649 ( $S=1$  for the untreated group), and then we calculate the geometric mean for all tumors  
650 containing the sgID and Inert tumors across all mice in the group.

651 The score for the relative geometric mean is calculated as:

652

$$ScoreRGM_{i,j} = \log_2\left(\frac{GM_{i,j}/GM_{Inert,j}}{GM_{i,untreated}/GM_{Inert,untreated}}\right)$$

653 where  $GM_{i,j}$  is the geometric mean for tumors containing sgID  $i$  in treatment group  $j$  in the  
654 selected  $N$  tumors. Under the null hypothesis,  $ScoreRGM_{i,j} = 0$ . Under the alternative  
655 hypothesis where  $ScoreRGM_{i,j} \neq 0$ , a positive sign of  $ScoreRGM_{i,j}$  suggests that the tumors  
656 with a particular sgID are more resistant than the Inert tumors, while a negative sign of the score  
657 suggests that these tumors are more sensitive than the Inert tumors.

658 **Evaluating whether ScoreRTN and ScoreRGM are biased**

659 To test whether either statistic is biased, we calculate the *ScoreRTN* and *ScoreRGM* using  
660 untreated mice subjected to a simulated treatment with no GSTR (specifically, the 5 untreated  
661 mice from the palbociclib repeat experiment). This represents an ideal scenario where we know  
662 exactly how each tumor responded to the treatment (because we generate the responses through  
663 simulations), and we are able to measure the exact tumors with and without treatment.  
664 Specifically, as shown in **Supplementary Fig. 3a**, we reduce the tumor sizes of all tumors in the  
665 five untreated mice by 50% as the “treated” tumors (**Supplementary Fig. 3b**). For a biased  
666 method illustrated in **Supplementary Fig. 3c, e, f**, which fails to consider the size reduction of  
667 tumors due to drug treatment by using the constant 1000 cell cutoff in both untreated and treated  
668 mice, the relative tumor number and relative geometric mean does not remain constant between  
669 treated and untreated mice (**Supplementary Fig. 3e, f**). This is because a constant cell number  
670 cutoff effectively compares different proportions of the distributions of the inert and TS-  
671 inactivated tumors in the treated and untreated mice.

672 On the other hand, using the adaptive cutoff method introduced above, no false signals of  
673 *ScoreRTN* and *ScoreRGM* were observed (**Supplementary Fig. 3d, g, h**), because we are  
674 comparing the matched portions of the distributions for the Inert tumors and tumors of each  
675 genotype (tumor with each sgID) between untreated and treated mice. Therefore, these two  
676 statistics appear unbiased.

677 **Bootstrapping the tumors**

678 When generating null distributions of scores and calculating the p-values, we performed  
679 bootstrap resampling on tumors. During bootstrapping, we consider tumor size variations both  
680 across mice and within a mouse using a nested resampling approach: first, we bootstrapped mice  
681 in the untreated and/or the treated group to generate pseudogroups of mice, and then within each  
682 mouse, we bootstrapped all observed tumors carrying each sgID.

683 **Generate a null distribution of *ScoreRGM* and *ScoreRTN***

684 To generate a null distribution of *ScoreRTN* and *ScoreRGM* in the absence of GSTR, we  
685 sampled with replacement the same number of mice as in the treated group from the 8 untreated  
686 mice and applied estimated drug effects  $S$  on the tumors from the “treated” groups. For each  
687 bootstrap run, we re-estimated  $S$  and calculated the values of *ScoreRTN* and *ScoreRGM*.

688 **Generate the observed distribution and calculation of the confidence interval for each score**

689 To calculate the confidence interval for each score, we bootstrapped mice in the treated  
690 and untreated groups, respectively, and then re-calculated  $S$ , *ScoreRTN*, and *ScoreRGM*. The  
691 bootstrap process was performed 10,000 times, and the 95% confidence interval of each score  
692 was calculated as the 2.5%ile, and 97.5%ile of the bootstrapped results.

693 **Calculation of the *P*-value for *ScoreRTN* and *ScoreRGM***

694 To see how the distribution of observed *ScoreRTN* and *ScoreRGM* of sgID  $i$  deviates  
695 from the null distribution, we compared the distribution of the two observed scores to that  
696 calculated from (1) simulated data with no *GSTR* for all sgIDs and to (2) simulated data with no  
697 *GSTR* for sgID  $i$  to determine the *P*-value. For each comparison, we sample values from both  
698 distributions and calculate the *P*-value as the fraction of times when their differences are not in  
699 the same direction as the observed score, *i.e.*, how often do we see equal or more extreme scores  
700 under the null distribution. To be conservative, the maximum of the two *P*-values calculated  
701 from the two comparisons were reported as the *P*-value. This bootstrap process is performed  $10^8$   
702 times to calculate the *P*-values.

703 **Power analysis for *ScoreRTN* and *ScoreRGM* in our study**

704 To estimate the sensitivity (True Positive Rate) and specificity (1-False Positive Rate) of  
705 our study (**Fig. 2b, c**), we sampled with replacement eight and five mice (minimum number of  
706 treated mice in the pharmacogenetics mapping experiment) from the eight untreated mice, as the  
707 “untreated” and “treated” groups, respectively. We then reduce all tumor sizes to 50% as the  
708 drug effect ( $S=0.5$ ) and apply an input  $G = -50\%, -20\%, 0\%$  (no genotype-specific drug  
709 response), 10%, 20%, and 50% to each non-Inert sgIDs by additionally changing each tumor  
710 sizes by the corresponding proportions. For instance,  $G=20\%$  means the overall drug effect on  
711 tumors carrying the sgRNA is  $(1-50\%) \times (1+20\%) = 60\%$ . Sensitivity is calculated as the  
712 probability of detecting preassigned true genotype-specific interactions, and specificity is  
713 calculated as the proportion of sgIDs correctly identified as having no *GSTR* when  $G = 0$ . A total  
714 of 100 runs of simulations of the 11 tumor suppressor gene targeting sgIDs were performed for

715 each preassigned  $G$ . We adjust the cutoff for  $P$ -values and calculated a series of sensitivity and  
716 specificity values to plot the receiver operating characteristic (ROC) curve.

717 **Power analysis for *ScoreRTN* and *ScoreRGM* for various sample sizes**

718 To evaluate the power of our method using various sample sizes (**Supplementary Fig 4**),  
719 we sampled the same number of mice (5, 10, or 20 mice) with replacement from the 8 untreated  
720 mice as the untreated and treated group. Similar to the previous section of Power analysis using 8  
721 and 5 mice respectively for untreated and treated mice, we apply  $G$  of various magnitudes and  
722 plotted the ROC curve when we use 5, 10, and 20 mice for each group in our experiment,  
723 respectively.

724 **Power analysis for *ScoreRTN* and *ScoreRGM* for tumor size-dependent GSTR**

725 We evaluate the effectiveness of *ScoreRTN* and *ScoreRGM* in capturing GSTR when the  
726 input  $G$  is not a constant factor constant across tumors with various sizes (**Supplementary Fig.**  
727 **5**). We apply a truncated effect of  $G$  where 1) only tumors smaller than 4000 cells showed  
728 genotype-specific sensitivity or 2) only tumors larger than 4000 cells showed genotype-specific  
729 resistance. The rest of the tumors are simulated to respond the same as Inert tumors to the drug.  
730 We calculated the ROC curves for the two statistics using 5 mice in both the untreated and  
731 treated groups.

732 Apart from *ScoreRTN* and *ScoreRGM*, which are based on the relative tumor number and  
733 relative geometric mean, other summary statistics, such as **relative LN mean** (*ScoreRLM*), can  
734 also be used to identify GSTR. The score for the relative LN mean is calculated as:

$$735 \quad ScoreRLM_{i,j} = Log_2\left(\frac{LN \text{ mean}_{i,j} / LN \text{ mean}_{Inert,j}}{\frac{LN \text{ mean}_{i,\text{untreated}} / LN \text{ mean}_{Inert,\text{untreated}}}{LN \text{ mean}_{Inert,\text{untreated}}}}\right)$$

736 where  $\text{LN mean}_{i,j}$  is the LN mean for tumors containing sgID  $i$  in treatment group  $j$  in the  
737 selected  $N$  tumors. We compared and contrasted the performance of the three metrics when the  
738 GSTR is not a constant factor, and show that if we have a good reason to believe that only very  
739 large tumors show genotype-specific responses,  $\text{ScoreRLM}$  is the best metric among the three.  
740 Otherwise, the other two metrics,  $\text{ScoreRTN}$  and  $\text{ScoreRGM}$ , will outperform  $\text{ScoreRLM}$ .

741 **Evaluating whether inaccuracy of drug effect ( $S$ ) estimation influences estimates of GSTR**

742 We also evaluate the impact of inaccurately estimating drug effects on our estimates of  
743 GSTR (**Supplementary Fig. 9**). Instead of estimating the effect size as described in section  
744 “calculation of proportional size-reduction as drug effect”, we assign  $S$  to be a constant value,  
745 taking three discrete values 0.3, 0.5, and 0.7 when we know the simulated truth of drug effect is  
746  $S=0.5$ . For each simulated scenario, we calculated the specificity and sensitivity and plotted the  
747 ROC curve for detecting  $G=+20\%$  using 5 mice in both the untreated and treated groups  
748 (**Supplementary Fig 9**).

749 **Calculating ScoreGSTR ( $\hat{G}$ ) as the combined score**

750 Although  $\text{ScoreRTN}$  and  $\text{ScoreRGM}$  may have an emphasis on different aspects of GSTR  
751 on tumor size distribution, it would be helpful to have a single combined score. We calculated a  
752 combined score of GSTR ( $\hat{G}$ ) by taking the inverse variance weighted average of  $\text{ScoreRTN}$  and  
753  $\text{ScoreRGM}$ , then converting it to the linear scale (**Fig 2f, Supplementary Fig 4c**).

754 
$$\text{ScoreGSTR} = \left( \frac{\text{ScoreRTN}}{\sigma_{\text{ScoreRTN}}^2} + \frac{\text{ScoreRGM}}{\sigma_{\text{ScoreRGM}}^2} \right) / \left( \frac{1}{\sigma_{\text{ScoreRTN}}^2} + \frac{1}{\sigma_{\text{ScoreRGM}}^2} \right)$$

755 
$$\hat{G} = 2^{\text{ScoreGSTR}} - 1$$

756 If  $\hat{G}>0$ , GSTR is resistant, and if  $\hat{G}<0$ , GSTR is sensitive.

757 To be very conservative, for the combined score to be called significant, we require at  
758 least one significant  $P$ -value ( $P < 0.05$ ), and one marginally significant  $P$ -value ( $P < 0.1$ ) for the  
759 two statistics *ScoreRTN* and *ScoreRGM*.

760 **Evaluate the consistency for choosing various cell cutoffs and control sgIDs**

761 We use a cutoff of 1000 cells for most parts of the analysis, but we also wanted to  
762 evaluate whether our results are robust to using higher and lower cell number cutoffs. Therefore,  
763 we adjusted the cutoff to 500 cells and 1500 cells and re-identified the significant GSTR under  
764 each scenario (**Supplementary Fig. 8a**).

765 For most analyses, we aggregate tumors with *sgNeo1*, *sgNeo2*, *sgNeo3*, and *sgNT1* as a single  
766 Inert control sgRNA to determine the baseline. We also explored whether excluding any of the  
767 four sgIDs associated with Inert sgRNAs from the control group would yield similar results. For  
768 comparison, we calculated the Spearman correlation and linear correlation, identified significant  
769 cases of GSTR, and the overall direction of GSTR for each scenario compared with using all  
770 four sgIDs associated with Inert sgRNA.

771 **Comparing with human cell line response data**

772 The drug sensitivity data from human cell lines were downloaded from the Genomics of  
773 Drug Sensitivity in Cancer (GDSC) database ([www.cancerrxgene.org](http://www.cancerrxgene.org))<sup>3</sup>. GDSC used logic-based  
774 modeling to quantified how genetic alterations in 1001 human cancer cell lines are correlated  
775 with sensitivity to various drugs. There is a limited number of LUAD cell lines in the database.  
776 Therefore, we focused on comparing the results from Pan-cancer cell lines. All 5 monotherapies  
777 used in our study were assessed by GDSC. Except for *Keap1* and *Rbm10*, which are not reported

778 for everolimus and paclitaxel, the GSTR of all other 51 gene-drug pairs were quantified by  
779 GDSC. The effect size and FDR-corrected *P*-values were used for comparison.

780 **Hierarchical clustering of *GSTR* for treatment and genes**

781 To better visualize the similarity of the *GSTR* profiles, we performed hierarchical  
782 clustering with complete linkage on  $\hat{G}$  to visualize the relationship across different genes and  
783 across different therapies (**Supplementary Fig 7c, d**). Therapies or genes that are similar to each  
784 other in genotype-specific responses are clustered together.

785 **Analysis of clinical data for resistance to chemotherapy**

786 Patients with metastatic or recurrent lung adenocarcinoma harboring a KRAS mutation in  
787 codons 11, 12, or 61, as detected by MSK-IMPACT<sup>31</sup>, were reviewed. Patients who received  
788 platinum chemotherapy (carboplatin or cisplatin) with pemetrexed +/- bevacizumab as first-line  
789 treatment were included (n = 216). Treatment efficacy was measured as time of first treatment  
790 with platinum doublet chemotherapy to start of next systemic therapy, or death if no subsequent  
791 therapy was received. Patients who continued on platinum doublet therapy at the last follow up  
792 were censored. Data collection was approved by the MSK institutional review board.

793 Kaplan-Meier estimator plots of time-to-next-treatment for patients with and without  
794 mutations at each of the 11 tumor suppressor genes of interest were generated. In addition, a  
795 multivariable Cox proportional hazards model analysis was performed integrating the mutational  
796 status of the 11 genes as individual input features to assess the independent effect of co-  
797 occurring mutations.

798

799

800 **FIGURE LEGENDS**

801 **Fig. 1. Optimization of tumor-barcoding coupled with high-throughput barcode sequencing**  
802 **(Tuba-seq) for the analysis of genotype-specific therapy responses (GSTRs) *in vivo*.**

803 **a.** Overview of Tuba-seq pipeline to uncover GSTRs. The Lenti-TS<sup>Pool</sup>/Cre viral pool contains  
804 barcoded vectors with sgRNAs targeting 11 putative tumor suppressors that are frequently  
805 mutated in human lung adenocarcinoma. Tumors are initiated in either *Kras*<sup>LSL-G12D/+</sup>;R26<sup>LSL-Tom</sup>  
806 (*KT*) or *Kras*<sup>LSL-G12D/+</sup>;R26<sup>LSL-Tom</sup>;H11<sup>LSL-Cas9</sup> (*KT;H11<sup>LSL-Cas9</sup>*) mice. Following tumor  
807 development, mice are treated with therapies, and barcode sequencing libraries are prepared from  
808 each tumor-bearing lung.

809 **b.** Comparison of our current pipeline with our previous Tuba-seq pipeline (Rogers et al. 2017).

810 **c.** Stringent filtering effectively eliminated spurious tumors. Analysis of the barcodes associated  
811 with the sgID specific for the Spike-in control cells (3 cell lines with a defined sgID-BC added at  
812 5x10<sup>5</sup> cell/sample as the benchmark) enables identification of recurrent barcode reads generated  
813 from sequencing and other errors (Spurious tumors). Data is from a typical lane of 22  
814 multiplexed Tuba-seq libraries from *KT;H11<sup>LSL-Cas9</sup>* mice with Lenti-TS<sup>Pool</sup>/Cre initiated tumors.

815 **d.** The percent of tumors with barcodes validated within the lentiviral plasmid pool is constant  
816 across tumor sizes. As sequencing and other processing errors are most likely to create small  
817 spurious tumors, this finding suggests that tumors detected by Tuba-seq represent real clonal  
818 expansions of barcoded cells.

819 **e.** The relative size of tumors of each genotype in *KT;H11<sup>LSL-Cas9</sup>* mice 18 weeks after tumor  
820 initiation with Lenti-sgTS<sup>Pool</sup>/Cre. The relative sizes of tumors at the indicated percentiles were  
821 calculated from the tumor size distribution of all tumors in 5 mice. Error bars show 95%  
822 confidence intervals.

823

824 **Fig. 2. Tuba-seq quantifies genotype-specific therapeutic responses (GSTR) for multiple**  
825 **therapies.**

826 **a.** Data analysis pipeline to identify GSTR by comparing the relative tumor number (*ScoreRTN*)  
827 and relative geometric mean (*ScoreRGM*) between tumors containing a tumor suppressor  
828 targeting sgRNA and Inert tumors in the untreated and treated mice.

- 829   **b.** The sensitivity and specificity of *ScoreRTN* estimated from simulations of preassigned drug  
830   effect ( $S=0.5$ ) and GSTR (various  $G$ ). There is no genotype-specific response when  $G=0$ .  $G$  of -  
831   20% means the tumors with the sgRNA were reduced by an additional 20% in size.
- 832   **c.** The sensitivity and specificity of *ScoreRGM* estimated from the same simulation as in b.
- 833   **d.** Likely mechanism of action for monotherapies used for treatments.
- 834   **e.** Timeline of the experiment. Tumors were initiated in *KT;H11<sup>LSL-Cas9</sup>* mice with the barcoded  
835   Lenti-sgTS<sup>Pool</sup>/Cre. Three weeks of treatment was initiated after 15 weeks of tumor growth.
- 836   **f-h.**  $\hat{G}$  calculated from the inverse variance weighted average of *ScoreRTN* and *ScoreRGM* for  
837   the pharmacogenomic mapping experiment (**f**), negative control experiment in *KT* mice (**g**) and  
838   palbociclib repeat experiment (**h**). Stars represent significant cases.
- 839   **i.** Comparison of our identified GSTRs with those from the Genomics of Drug Sensitivity in  
840   Cancer (GDSC) database. Stars represent significant cases.
- 841   **j.** Kaplan-Meier curve (with 95% confidence interval in shading) of time-to-next-treatment  
842   (months) for patients with or without *KEAP1* mutations with metastatic oncogenic *KRAS*-driven  
843   lung adenocarcinoma to platinum-containing chemotherapy. The number of patients in each  
844   group is shown.  $P$ -values were calculated from the Mantel-Haenszel test.
- 845   **k.** Responses of patients with metastatic oncogenic *KRAS*-driven lung adenocarcinoma to  
846   platinum-containing chemotherapy are consistent with *KEAP1* inactivation leading to resistance.  
847   *KEAP1* mutations are significantly correlated with a higher hazard ratio for time-to-next-  
848   treatment.

Li and Lin *et al.*

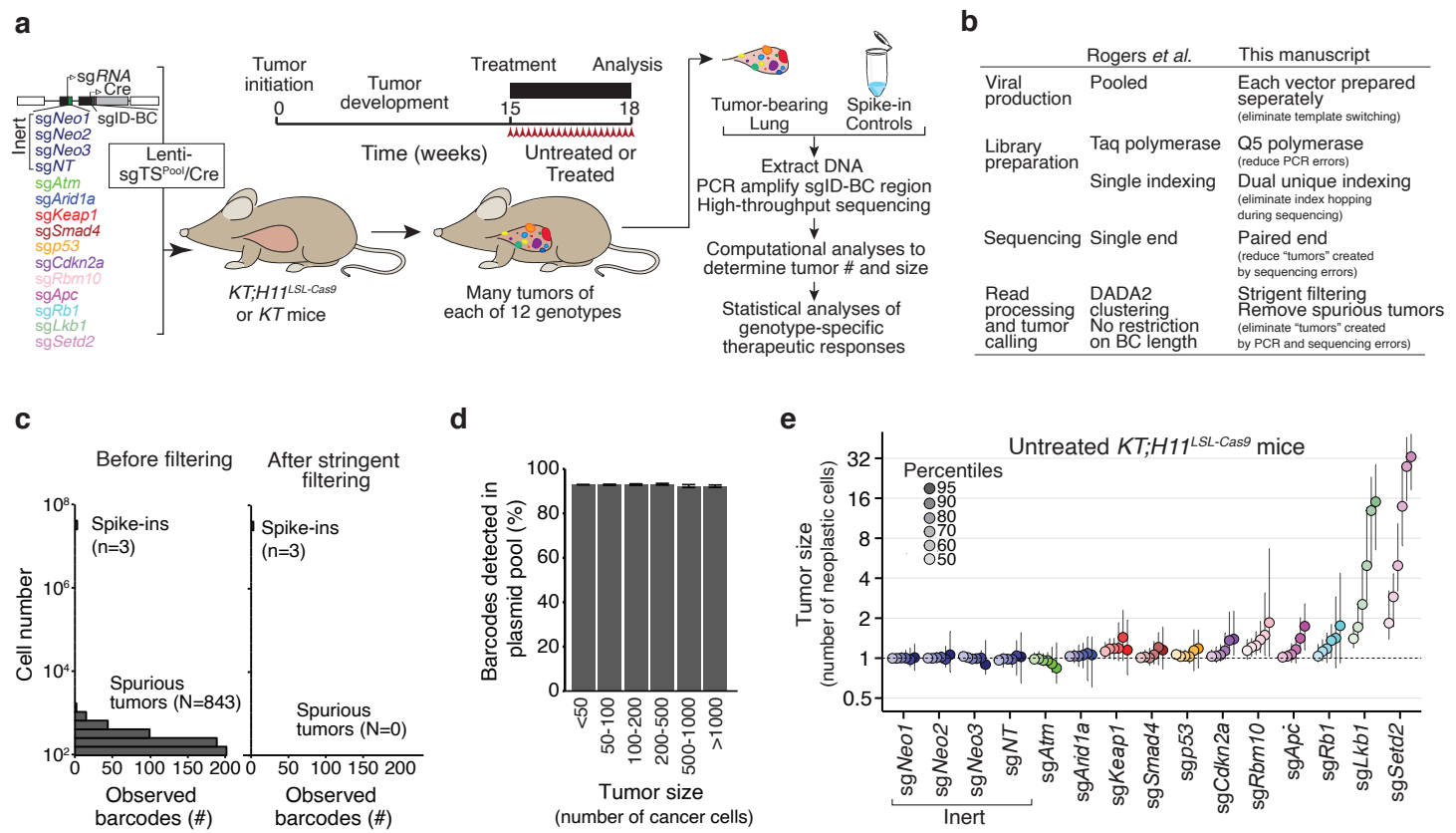


**Figure 1. Optimization of tumor-barcoding coupled with high-throughput barcode sequencing (Tuba-seq) for the analysis of genotype-specific therapy responses (GSTRs) in vivo.**

- a. Overview of Tuba-seq pipeline to uncover GSTRs. The Lenti-TS<sup>Pool</sup>/Cre viral pool contains barcoded vectors with sgRNAs targeting 11 putative tumor suppressors that are frequently mutated in human lung adenocarcinoma. Tumors are initiated in either *Kras*<sup>LSL-G12D/+;R26<sup>SL-Tom</sup> (KT) or *Kras*<sup>LSL-G12D/+;R26<sup>SL-Tom</sup>;H11<sup>LSL-Cas9</sup> (KT;H11<sup>LSL-Cas9</sup>) mice. Following tumor development, mice are treated with therapies, and barcode sequencing libraries are prepared from each tumor-bearing lung.</sup></sup>
- b. Comparison of our current pipeline with our previous Tuba-seq pipeline (Rogers *et al.* 2017).
- c. Stringent filtering effectively eliminated spurious tumors. Analysis of the barcodes associated with the sgID specific for the Spike-in control cells (3 cell lines with a defined sgID-BC added at 5x10<sup>5</sup> cell/sample as the benchmark) enables identification of recurrent barcode reads generated from sequencing and other errors (Spurious tumors). Data is from a typical lane of 22 multiplexed Tuba-seq libraries from KT;H11<sup>LSL-Cas9</sup> mice with Lenti-TS<sup>Pool</sup>/Cre initiated tumors.
- d. The percent of tumors with barcodes validated within the lentiviral plasmid pool is constant across tumor sizes. As sequencing and other processing errors are most likely to create small spurious tumors, this finding suggests that tumors detected by Tuba-seq represent real clonal expansions of barcoded cells.
- e. The relative size of tumors of each genotype in KT;H11<sup>LSL-Cas9</sup> mice 18 weeks after tumor initiation with Lenti-sgTS<sup>Pool</sup>/Cre. The relative sizes of tumors at the indicated percentiles were calculated from the tumor size distribution of all tumors in 5 mice. Error bars show 95% confidence intervals.

Li, Lin et al.

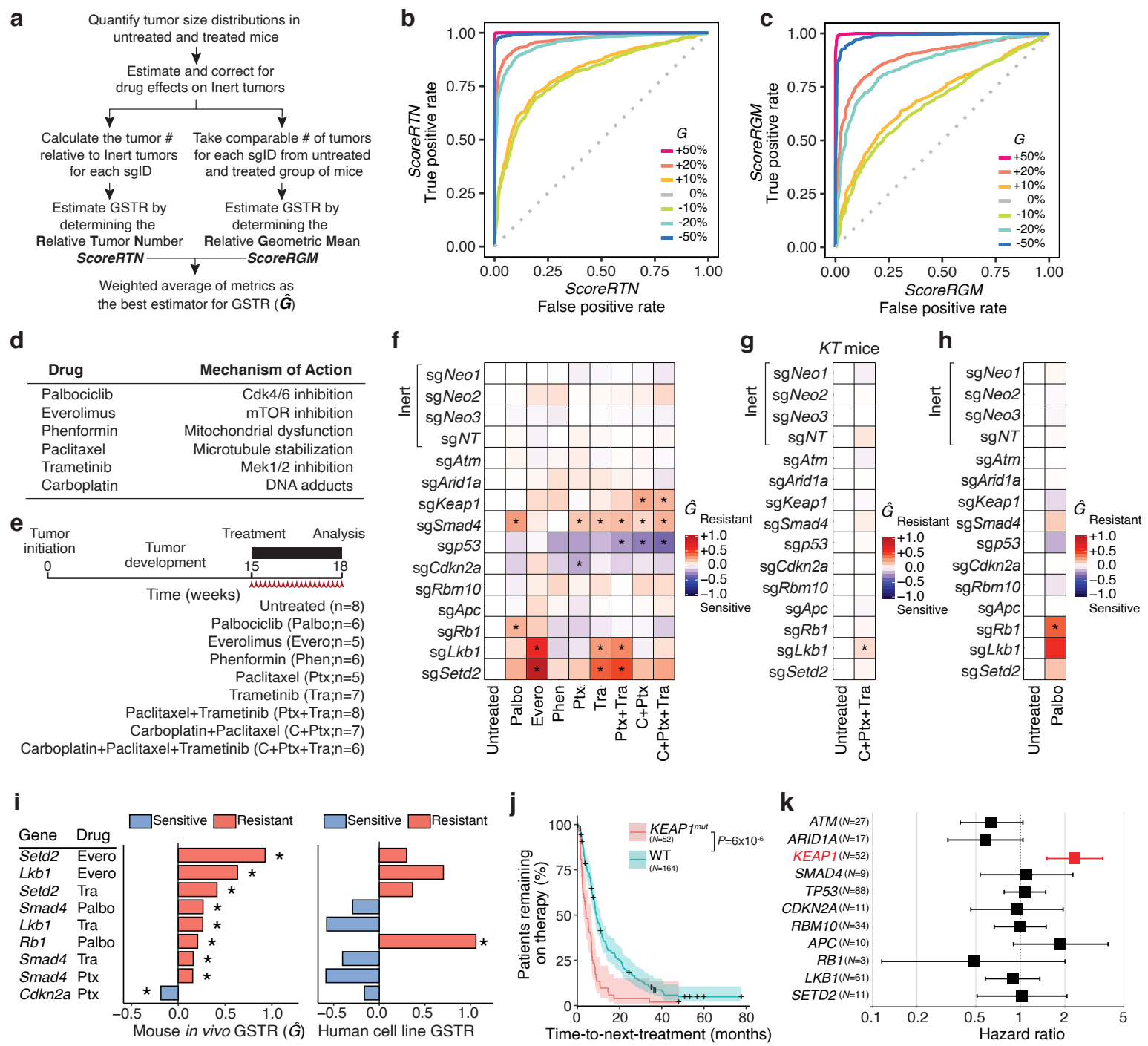
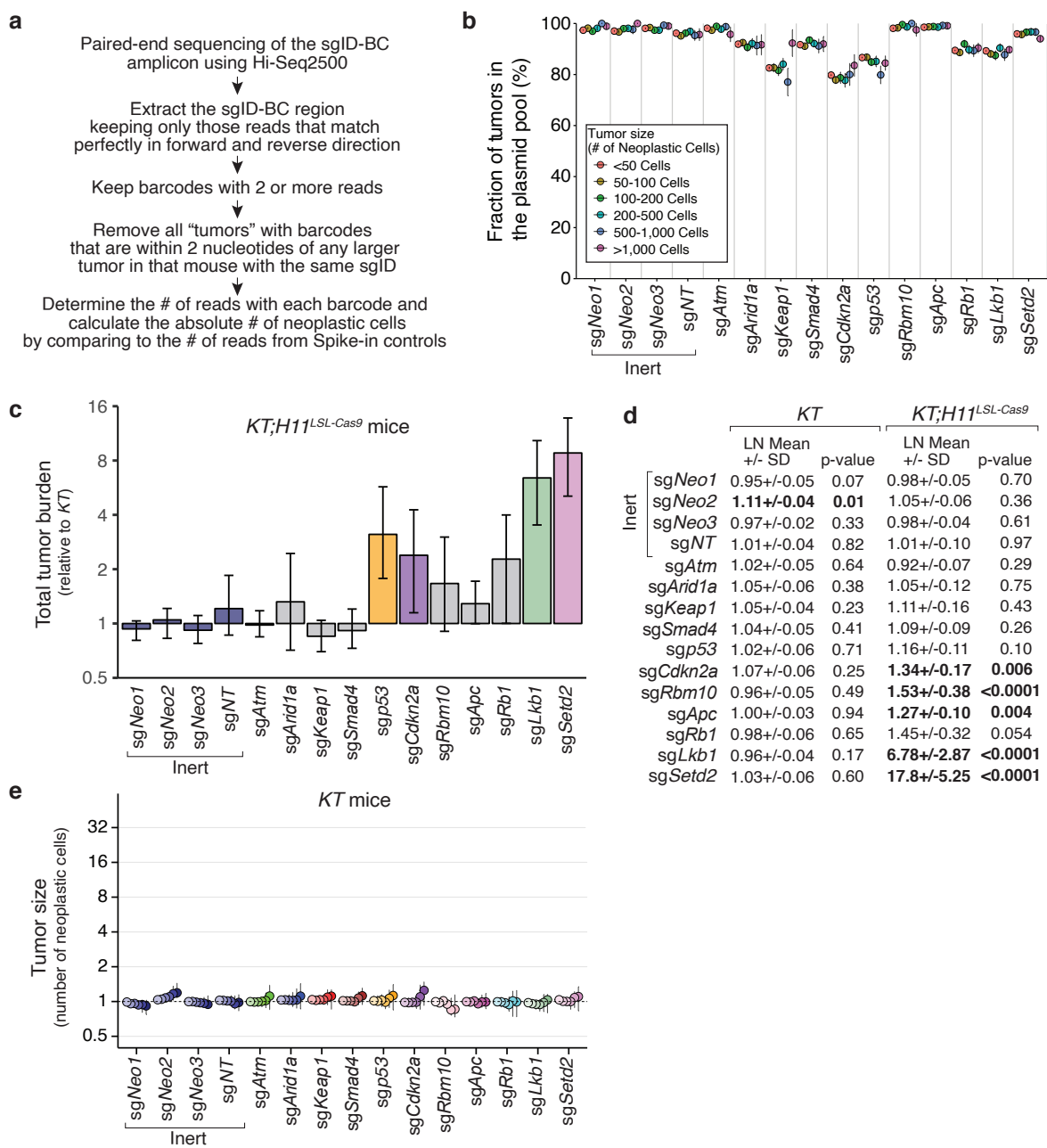


**Figure 2. Tuba-seq quantifies genotype-specific therapeutic responses (GSTR) for multiple therapies.**

- Data analysis pipeline to identify GSTR by comparing the relative tumor number ( $ScoreRTN$ ) and relative geometric mean ( $ScoreRGM$ ) between tumors containing a tumor suppressor targeting sgRNA and Inert tumors in the untreated and treated mice.
- The sensitivity and specificity of  $ScoreRTN$  estimated from simulations of preassigned drug effect ( $S=0.5$ ) and GSTR (various  $G$ ). There is no genotype-specific response when  $G=0$ .  $G$  of -20% means the tumors with the sgRNA were reduced by an additional 20% in size.
- The sensitivity and specificity of  $ScoreRGM$  estimated from the same simulation as in b.
- Likely mechanism of action for monotherapies used for treatments.
- Timeline of the experiment. Tumors were initiated in  $KT;H11^{LSL-Cas9}$  mice with the barcoded Lenti-sgTS<sup>Pool</sup>/Cre. Three weeks of treatment was initiated after 15 weeks of tumor growth.
- h.  $\hat{G}$  calculated from the inverse variance weighted average of  $ScoreRTN$  and  $ScoreRGM$  for the pharmacogenomic mapping experiment (f), negative control experiment in  $KT$  mice (g) and palbociclib repeat experiment (h). Stars represent significant cases.
- Comparison of our identified GSTRs with those from the Genomics of Drug Sensitivity in Cancer (GDSC) database. Stars represent significant cases.
- Kaplan-Meier curve (with 95% confidence interval in shading) of time-to-next-treatment (months) for patients with or without *KEAP1* mutations with metastatic oncogenic *KRAS*-driven lung adenocarcinoma to platinum-containing chemotherapy. The number of patients in each group is shown.  $P$ -values were calculated from the Mantel-Haenszel test.
- Responses of patients with metastatic oncogenic *KRAS*-driven lung adenocarcinoma to platinum-containing chemotherapy are consistent with *KEAP1* inactivation leading to resistance. *KEAP1* mutations are significantly correlated with a higher hazard ratio for time-to-next-treatment.

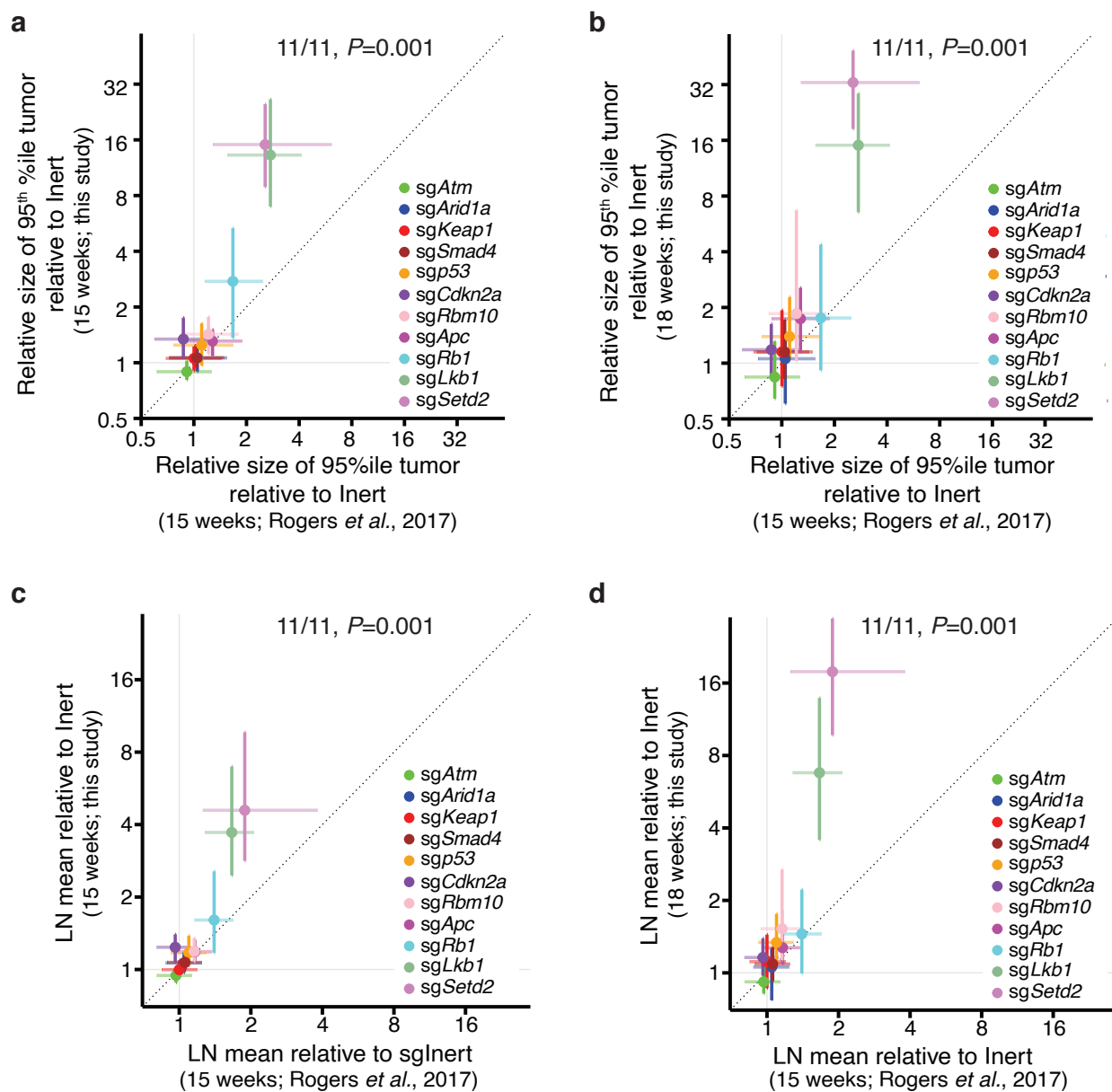
Li and Lin *et al.*



**Supplementary Figure 1. Optimization of Tuba-seq increases the resolution and precision of tumor analyses**

- a.** Overview of our new Tuba-seq analysis pipeline for calling sgID-BC from sequencing data and determining the number of neoplastic cells in each tumor (tumor size).
- b.** Fractions of tumor sgID-BC region recovered in the plasmid pool across multiple size ranges. By sequencing the sgID-BC region in the Lenti-sgRNA/Cre plasmids, we define a high confidence list of barcodes that are present in each sgID-BC region. If spurious tumor remains, the identified smaller tumors in *KT;Cas9* mice will less likely be uncovered in the plasmid pool compared with larger tumors. However, we find that equivalent proportions of tumors at all sizes are present in the plasmids pool. Note that not all barcodes found in tumors are found in the sequenced plasmids pool because the sequencing depth of the plasmid pool was insufficient to uncover all barcodes in the plasmid pools.
- c.** Total tumor burden in *KT;Cas9* mice with Lenti-TS<sup>Pool</sup>/Cre-initiated tumors relative to expected tumor burden calculated from *KT* mice. Error bars show 95% percent confidence intervals. Note that targeting p53 enables the generation of rare very large tumors, hence the tumor-suppressive effect of p53 is easily identified by this metric (which aggregates all cancer cells), while the 95<sup>th</sup> percentile of tumor size distribution and LN mean are much less dramatic.
- d.** The relative LN mean for tumors with each sgRNA in *KT* and *KT;H11<sup>LSL-Cas9</sup>* mice 18 weeks after tumor initiation normalized to that of all Inert tumors. Bootstrapped p-values are shown. P-values < 0.05, and their corresponding means are in bold.
- e.** The relative size of tumors initiated with each Lenti-sgRNA/Cre vector in *KT* mice 18 weeks after tumor initiation with Lenti-sgTS<sup>Pool</sup>/Cre. Relative size of tumors at the indicated percentiles within the distribution represent merged data from 4 mice. 95% confidence intervals are shown.

Li and Lin *et al.*

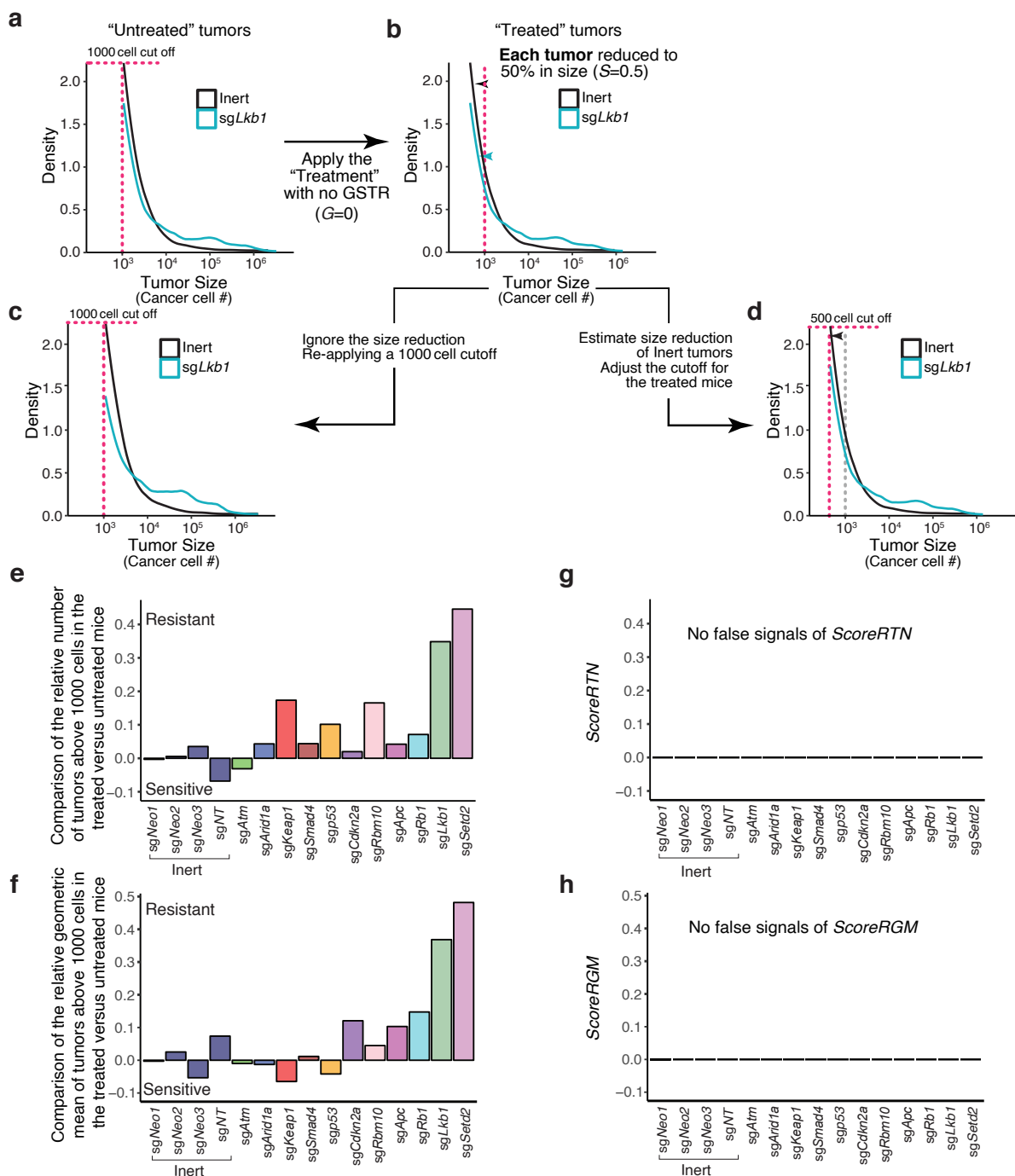


### Supplementary Figure 2. Optimization of Tuba-seq increases the resolution and precision of tumor analyses

**a,b.** Comparison of the relative 95<sup>th</sup> percentile tumor sizes (size of 95<sup>th</sup> percentile sgTS tumor/size of 95<sup>th</sup> percentile Inert tumor) of each genotype between the previous data (Rogers *et al.*, 2017) and the current data (this manuscript). Error bars show the 95% confidence interval. Current data from tumors 15 weeks (**a**) and 18 weeks (**b**) after tumor initiation are shown.

**c,d.** Comparison of the relative LN mean (LN mean of sgTS tumor/LN mean of Inert tumors) of the tumors of each genotype between the previous data (Rogers *et al.*, 2017) and the current data (this manuscript). Error bars show the 95% confidence interval. Current data from tumors 15 weeks (**c**) and 18 weeks (**d**) after tumor initiation is shown. In each panel, Error bars show the 95% confidence intervals. Dash lines represent equal detected magnitudes of tumor suppression across studies. 11/11 means 11 out of 11 the assayed genotypes showed a higher magnitude in current studies, and P-values are calculated from the sign-test of the difference in magnitudes for each metric between this study and the previous study.

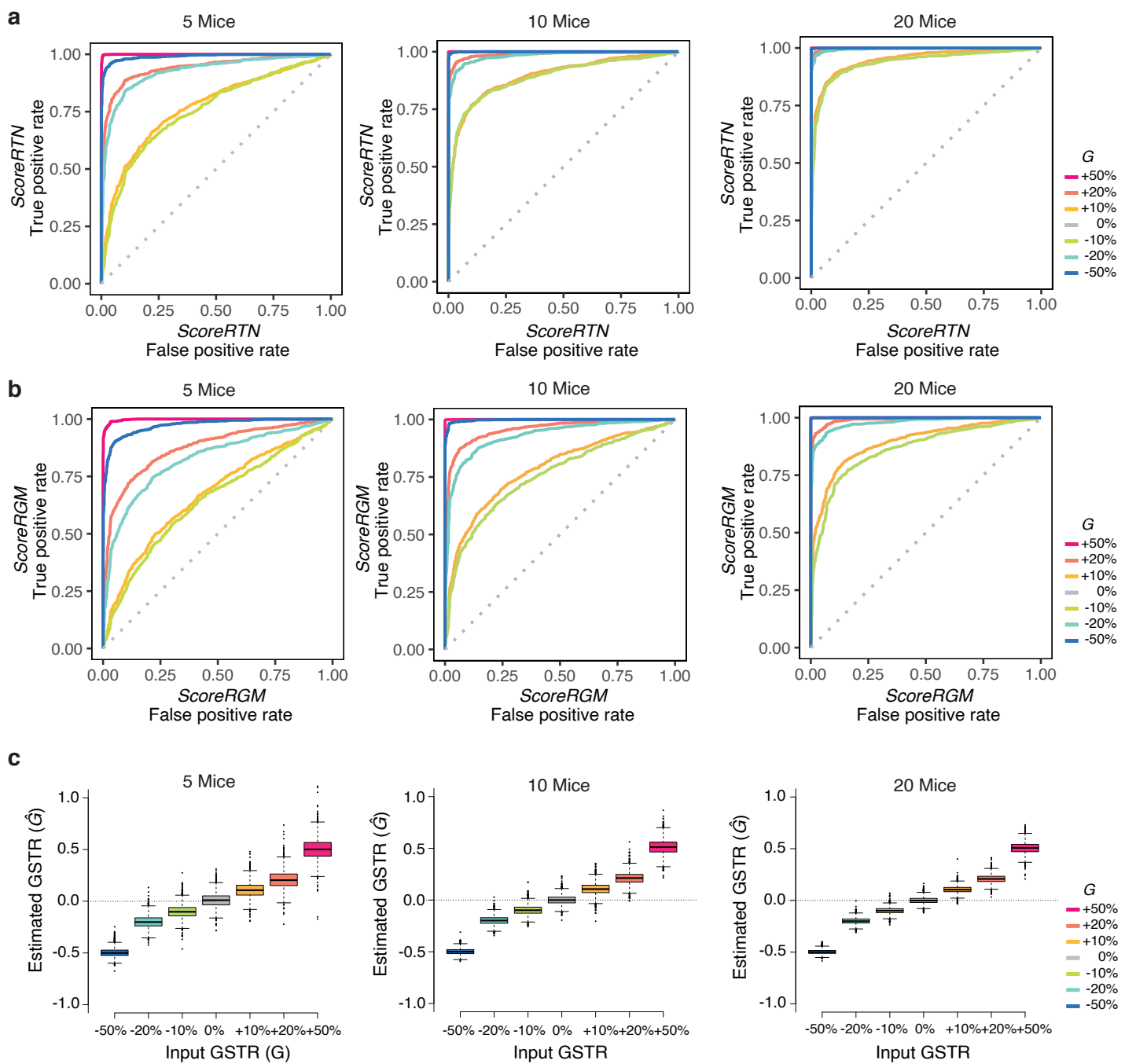
Li and Lin *et al.*



**Supplementary Figure 3. The intuitive approach of comparing tumors above a constant cutoff between the untreated and treated mice generates aberrant signals of Genotype-specific treatment responses (GSTRs)**

- a. Tumor size distributions of “untreated” Inert and sgLkb1 tumors were pooled from 5 *KT;Cas9* mice 18 weeks after tumor initiation for all simulations. Tumors with more than 1,000 neoplastic cells are plotted. Inert tumors are tumors containing sgNeo1, sgNeo2, sgNeo3, or sgNT. Targeting *Lkb1* changes the overall shape of the tumor size distribution.
- b. Tumor size distributions of “treated” Inert and sgLkb1 tumors were generated by reducing the size of every tumor to 50% ( $S=0.5$ ), assuming each cancer cell was killed by the drug with a 50% probability ( $G=0$ ).
- c. After re-applying a 1000 cell cut off, the new tumor size distributions of Inert and sgLkb1 tumors are noticeably different from those before the size reduction in panel a.
- d. To account for tumor size reduction, we need to adjust the cutoff in the treated group by the estimated size reduction due to treatment.
- e,f. Comparing the relative tumor number (e) and relative geometric mean (f) (normalized to the corresponding Inert tumors) between the “untreated” and “treated” tumors with each sgID by taking the  $\log_2$  ratio of the metric in the treated mice over that of the untreated mice for tumors with each sgID. The values are non-zero. Therefore, this intuitive approach is incorrect.
- g,h. After correcting for the overall tumor size reduction by the treatment, no false signals of ScoreRTN (g) and ScoreRGM (h) were generated when comparing the relative tumor number and relative geometric mean between the “untreated” and “treated” mice.

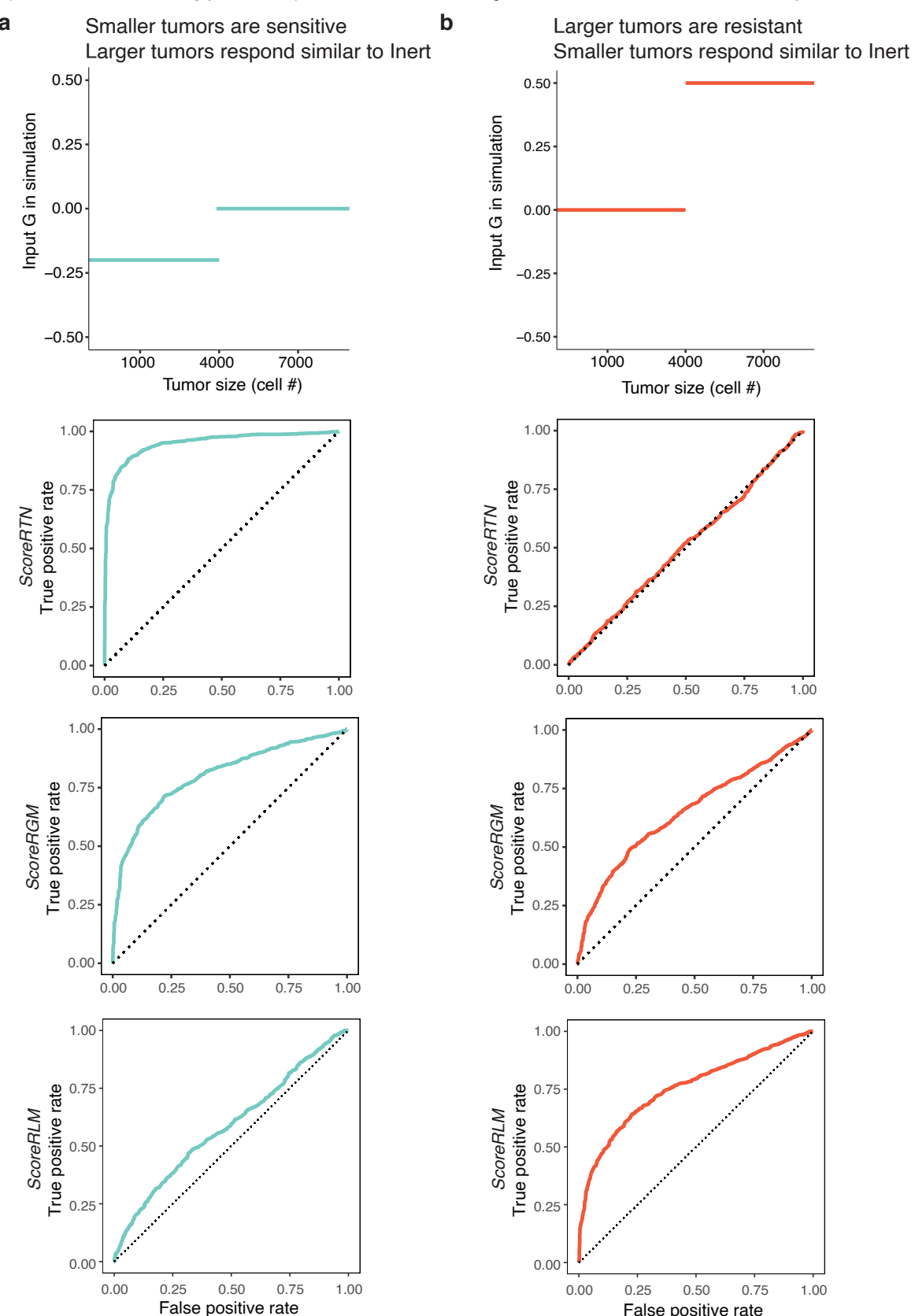
Li, Lin et al.



#### Supplemental Figure 4. Power analysis for various sample sizes.

- a.** The sensitivity and specificity of *ScoreRTN* estimated from simulation of preassigned drug effect ( $S=0.5$ ) and various input GSTR ( $G$ ) when various numbers of mice were used in the treated and untreated group (for example, “10 mice” means that 10 untreated and 10 treated mice were sampled from 8 untreated mice from the pharmacogenomic mapping experiment with replacement for simulation, respectively). The increase in sample size or input GSTR( $G$ ) leads to a higher power.
- b.** The sensitivity and specificity of *ScoreRGM* were estimated with the same parameter setting as in a.
- c.** Estimated GSTR ( $\hat{G}$ ) by combining *ScoreRTN* and *ScoreRGM* from the above simulations with various input GSTR ( $G$ ). The estimated GSTRs are unbiased and were more accurate with larger sample size.

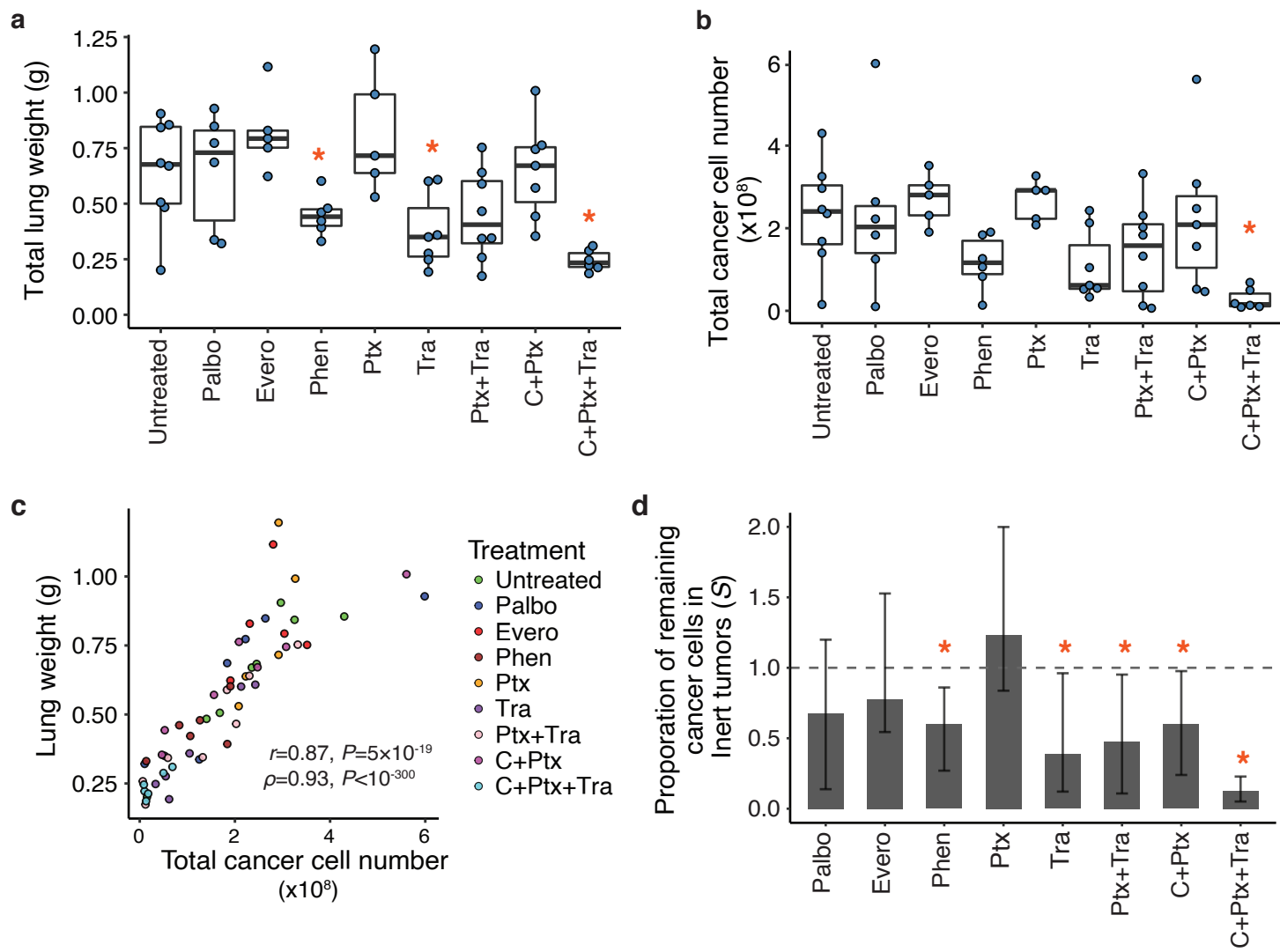
Li, Lin et al.



#### Supplemental Figure 5. Examples of scenarios where one score outperforms the other

- a.** Five untreated and treated mice were simulated as in Supplementary Fig 4 with  $S=0.5$ . The top panel shows the preassigned input GSTR ( $G$ ) on non-Inert tumors, where tumors smaller than 4000 cells showed an additional 20% reduction in size. When small tumors respond more, *ScoreRTN* outperforms *ScoreRGM* in detecting genotype-specific responses.
- b.** The simulation was the same as panel a except for the preassigned input GSTR. The top panel shows the input GSTR ( $G$ ), where tumors larger than 4000 cells respond less well to the drug compared with Inert tumors, resulting in tumors being 50% larger than expected when  $G=0$ . When large tumors respond less, *ScoreRTN* is not a sensitive metric to detect genotype-specific responses; however, *ScoreRGM* retains some power to detect genotype-specific responses. Other summary statistics, such as *ScoreRLM* that compares the relative LN mean for tumors between the treated and untreated mice, can also be used to identify GSTR. Compared with *ScoreRTN* and *ScoreRGM*, *ScoreRLM* has the lowest power when larger tumors respond similar to Inert tumors, and has the highest power when only larger tumors show GSTR.

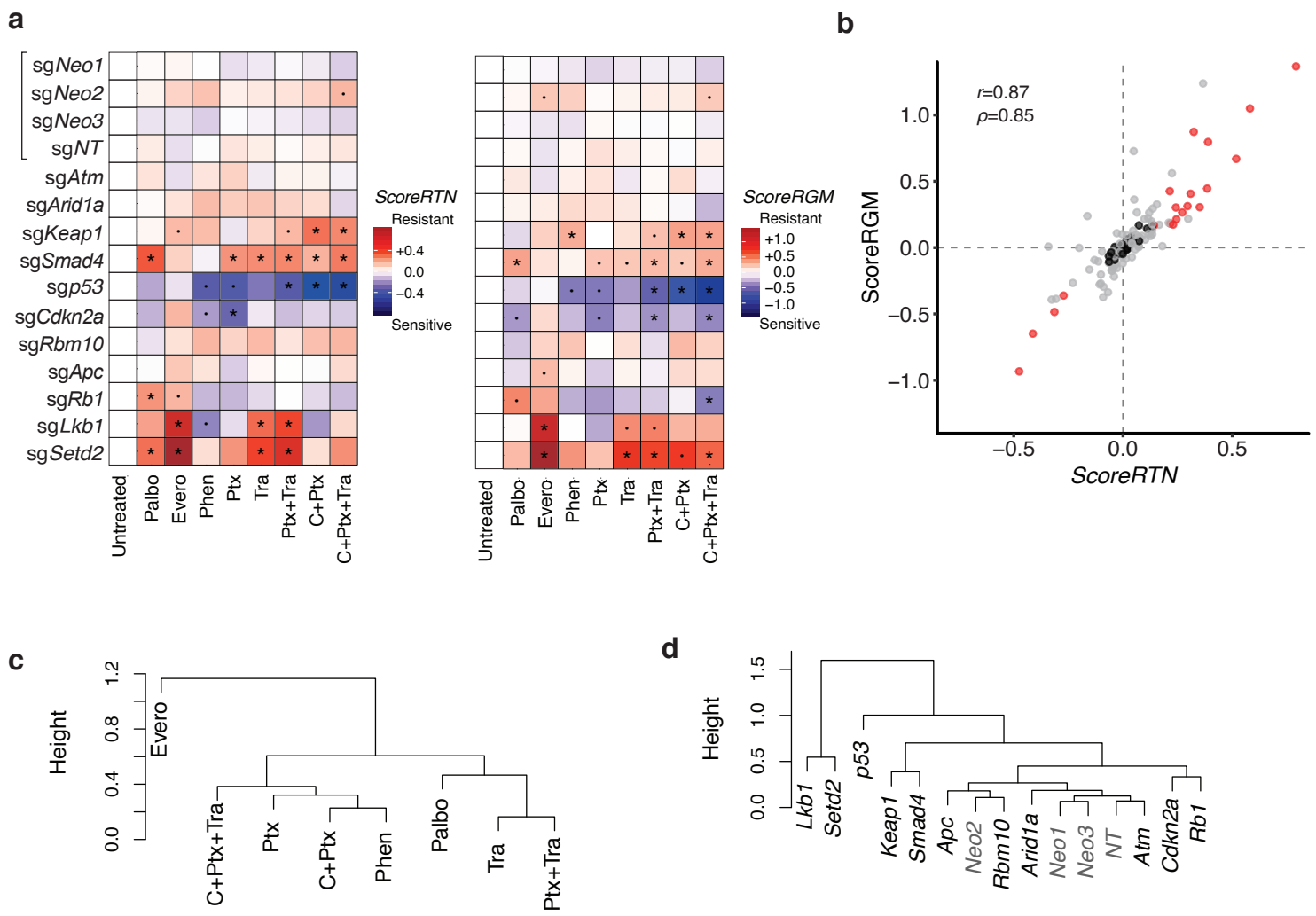
Li, Lin *et al.*



#### Supplemental Figure 6. Overall treatment responses of mice to therapies

- a. Boxplot showing the effects of treatment on mouse lung weight. Each blue dot is the lung weight of a mouse. Several treatments lead to reduced tumor burden sufficient to dramatically reduce total lung weight. Stars below the name of the treatment indicate significant reductions in lung weight by the treatment ( $P<0.05$ , Mann-Whitney U test).
- b. Boxplot showing the effect of treatment on the total cancer cell number. Each blue dot is the total cancer cell number of a mouse. The total cancer cell number in each lung was determined by converting the number of reads containing a sgID to cell number based on the read number of the three spike-ins with known cell number counts. Stars indicate significant reductions in total cancer cell number by the treatment ( $P<0.05$ , Mann-Whitney U test).
- c. Total lung weight is highly correlated with the total cancer cell number.
- d. The proportion of remaining cancer cells for Inert tumors  $S$  for each treatment is estimated by matching the distribution of Inert tumors in the treated and untreated mice. Stars indicate significant reductions in the remaining tumor cells ( $P<0.05$  by bootstrap).

Li, Lin et al.



### Supplemental Figure 7. ScoreRTN and ScoreRGM for all genotypes across all treatments and experiments

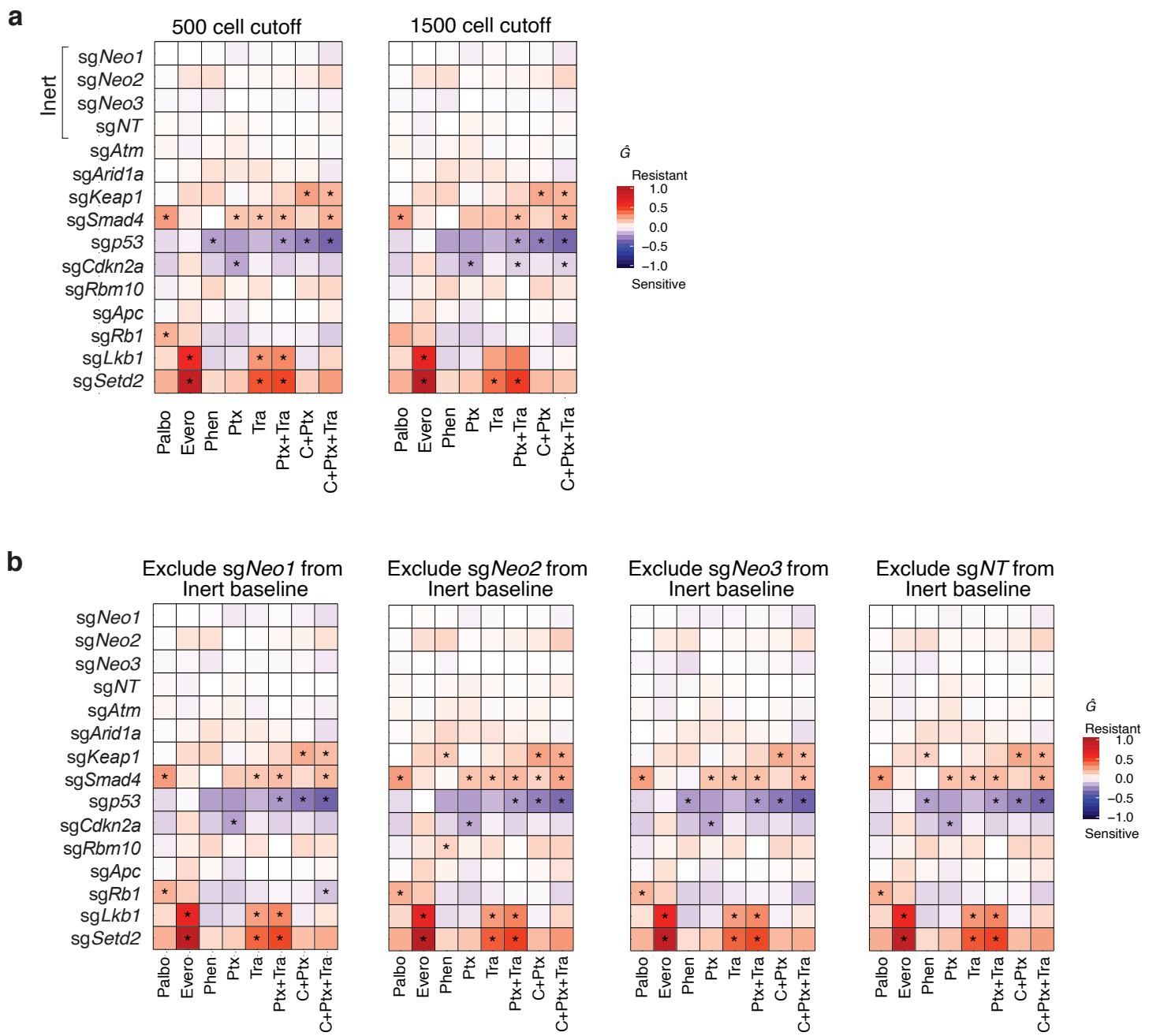
**a.** Heatmap for *ScoreRTN* and *ScoreRGM* for the pharmacogenomic mapping experiment outlined in Figure 2e. “.” indicates a marginally significant GSTR ( $P<0.1$ ), and “\*\*” indicates a significant GSTR ( $P<0.05$ ). *ScoreRTN* and *ScoreRGM* are integrated to generate  $\hat{G}$  shown in Figure 2f.

**b.** *ScoreRTN* and *ScoreRGM* are highly correlated. Red dots show interactions that are significant by one score and at least marginally significant by the other score. Gray dots are the rest of GSTR that doesn't fit the above criteria. Black dots show all GSTR for Inerts, all with small magnitudes and non-significant p-values.

**c.** Hierarchical clustering of the treatments in the pharmacogenomic mapping experiment based on  $\hat{G}$  with complete linkage. Combo treatments clustered close to their corresponding monotherapies.

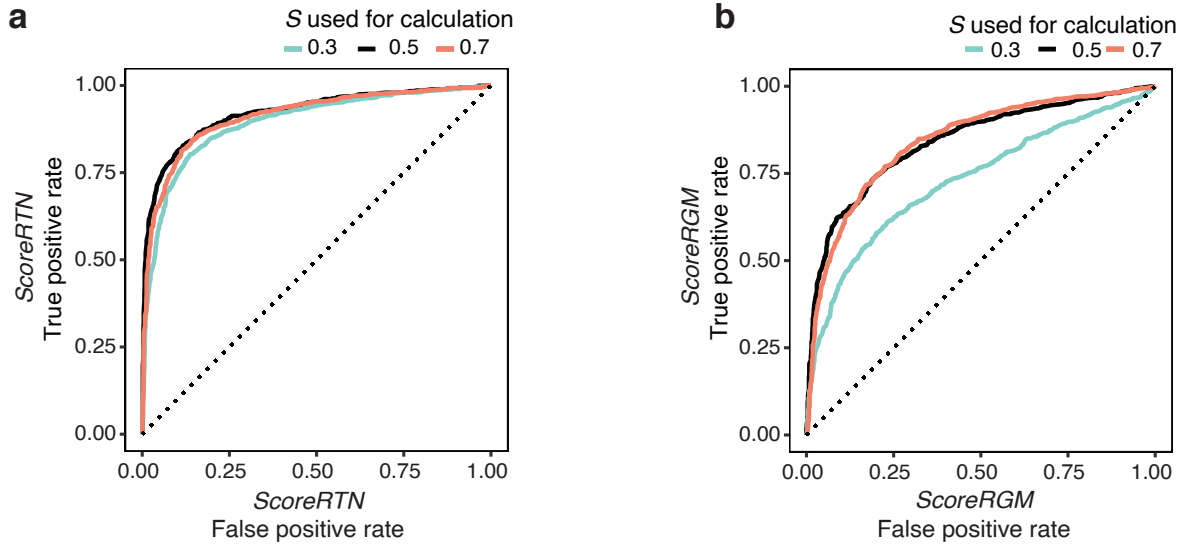
**d.** Hierarchical clustering of the genes in the pharmacogenomic mapping experiment based on  $\hat{G}$  with complete linkage. *Rb1* and *Cdkn2a* are in the same biological pathway and were clustered closely. *Lkb1* and *Setd2* were previously shown to be functionally redundant (Rogers et al. 2018) and were clustered closely.

Li, Lin et al.



**Supplemental Figure 8. Estimates of GSTRs are robust to changes in minimum tumor size cutoff and the composition of the Inert tumors**

- a. Throughout most analyses in this manuscript, we include tumors in untreated mice that are calculated to have over 1000 cells (a cutoff of 1000 cells). However, using 500 cells or 1500 cells as the tumor size cutoffs generated very similar results. The correlation between  $\hat{G}$  using 500 or 1500 cells as cutoff versus using 1000 cell cutoff was 0.998 and 0.997 for linear correlation, and 0.997 and 0.997 for rank correlation, respectively. Compared to using the original 1000 cell cutoff, 100% and 97.5% of the GSTR identified by  $\hat{G}$  were in the same direction, respectively. Among 19 significant GSTRs, 18 and 13 significant GSTRs were reidentified using the 500 and 1500 cell cutoff, respectively. Thus, the identified genotype-specific therapeutic responses are almost unaltered by using different cell number cutoffs. □
- b. Throughout most analyses in this manuscript, we aggregate tumors with sgNeo1, sgNeo2, sgNeo3 and sgNT as the Inert tumors. Excluding any of the Inerts yields similar results. The correlation between  $\hat{G}$  leaving out one of the Inerts versus using all four Inerts was over 0.998 for linear correlations and over 0.994 for rank correlations. Over 95.8% of the Significant  $\hat{G}$  results were in the same direction. At least 17 of the 19 significant GSTRs were reidentified in each setting.



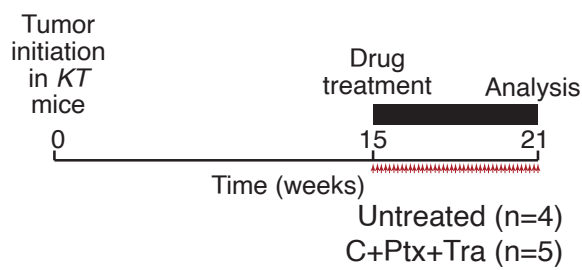
**Supplemental Figure 9. Estimates of GSTR by *ScoreRTN* and *ScoreRGM* are robust to inaccurate estimation of  $S$**

a. The calculation of *ScoreRTN* and *ScoreRGM* both depend on our estimate of the overall drug responses (represented as  $S$  - the remaining fraction of cancer cells for *Inert* tumors). In the simulation, we tested the impact of our estimates of  $S$  being inaccurate. Instead of estimating the effect size based on observed *Inert* tumors, we assign  $S$  to be a constant value, taking three discrete values 0.3, 0.5, and 0.7 when we know the preassigned drug effect is 0.5. ROC curves were plotted for detecting GSTRs with Input GSTR ( $G$ )=0.2. Incorrect estimation of  $S$  only slightly impacts the power of *ScoreRTN*.

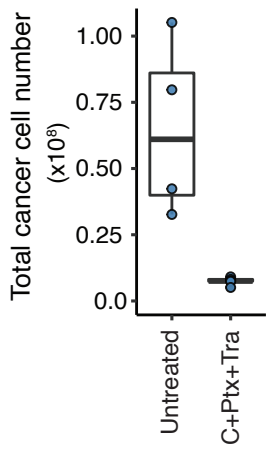
b. Similar simulation is performed for *ScoreRGM* and Incorrect estimation of  $S$  only slightly impacts the power of *ScoreRGM*.

Li, Lin *et al.*

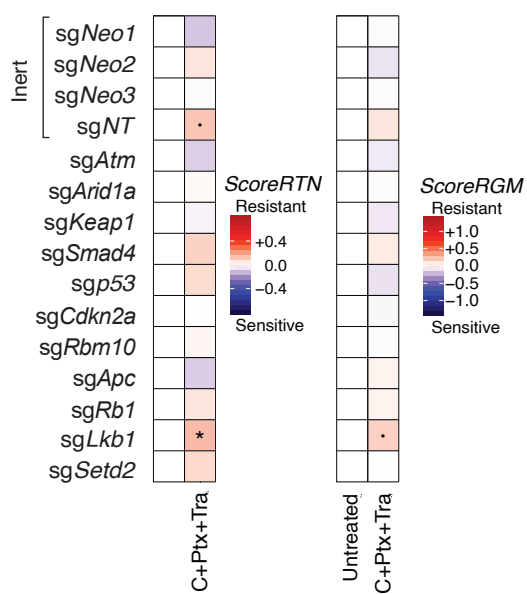
**a**



**b**



**c**



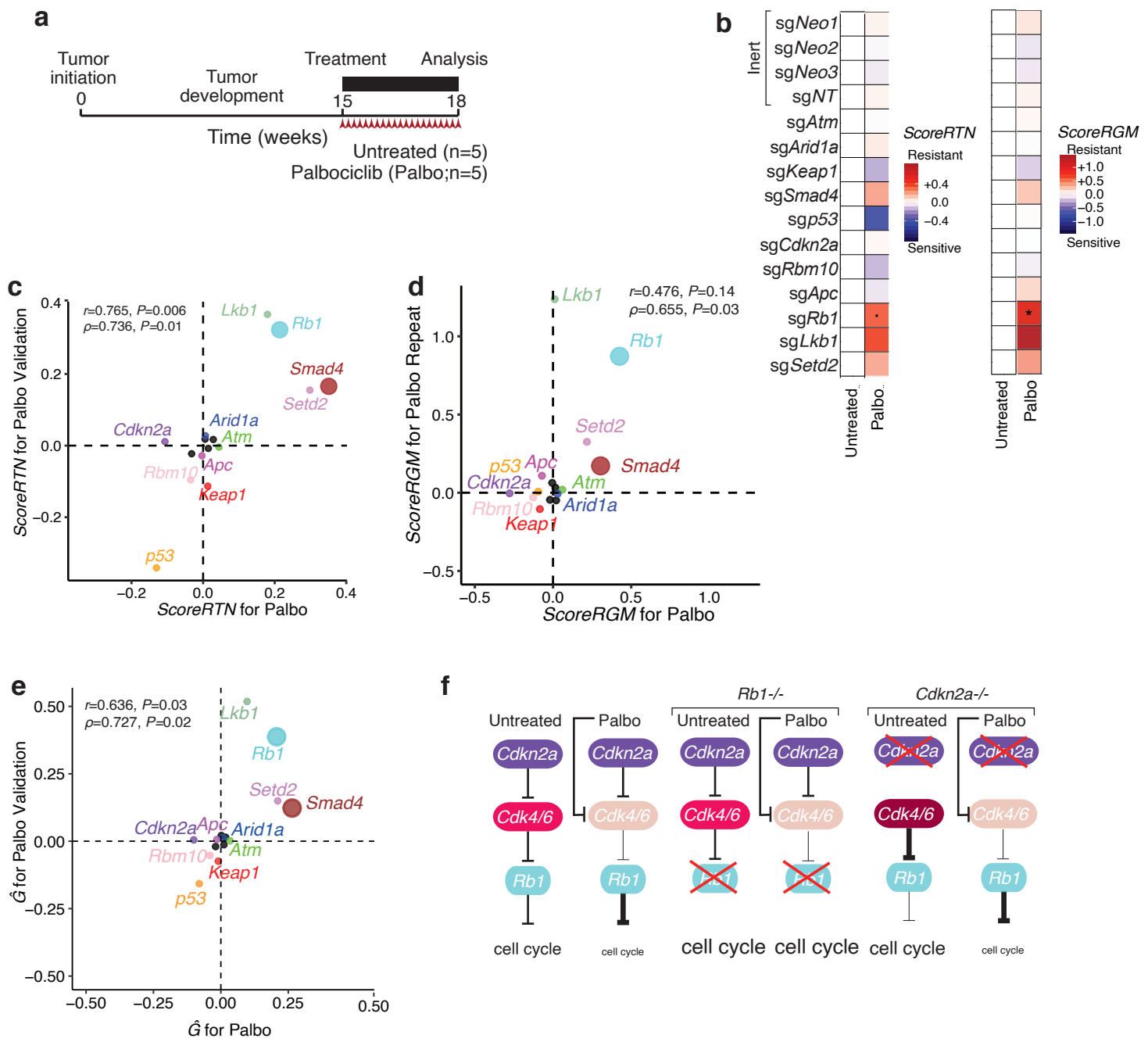
**Supplemental Figure 10. Only 1 weak GSTRs were identified in the negative control experiment in *KT* mice without Cas9.**

**a.** Outline of a negative control experiment. In this negative control experiment, we initiated tumors in *KT* mice (which lack Cas9) with Lenti-TSPool/Cre followed by a 6-week treatment with Carboplatin+Paclitaxel+Trametinib (C+Ptx+Tra). We chose this treatment, and prolonged treatment time, to generate maximal tumor responses which would most stringently test our analytical models. Given that the mice lack Cas9, all sgRNA are functional Inert, and we expected to find no differences in responses of tumors with different sgRNAs. The number of mice in each group is indicated.

**b.** Boxplot showing the effect of treatment on the total cancer cell number. Each blue dot is the total cancer cell number of a mouse. The total cancer cell number in each lung was determined by converting the number of reads containing a sgID to cell number based on the read number of the three spike-ins with known cell number counts. The total cancer cell numbers were significantly different across the two groups.

**c.** Heatmap for ScoreRTN and ScoreRGM for the negative control experiment. “.” indicates a marginally significant GSTR ( $P<0.1$ ), and “\*\*” indicates a significant GSTR ( $P<0.05$ ). Note the relatively low magnitudes of estimated effect relative to those shown in Supplementary Figure 7a. ScoreRTN and ScoreRGM are integrated to generate  $\hat{G}$  shown in Figure 2g. Apart from tumors with *sgLkb1* showing significant and marginally significant GSTRs with small magnitudes by ScoreRTN and ScoreRGM, respectively, other genes were non-significant when comparing the C+Ptx+Tra treated mice to untreated *KT* mice.

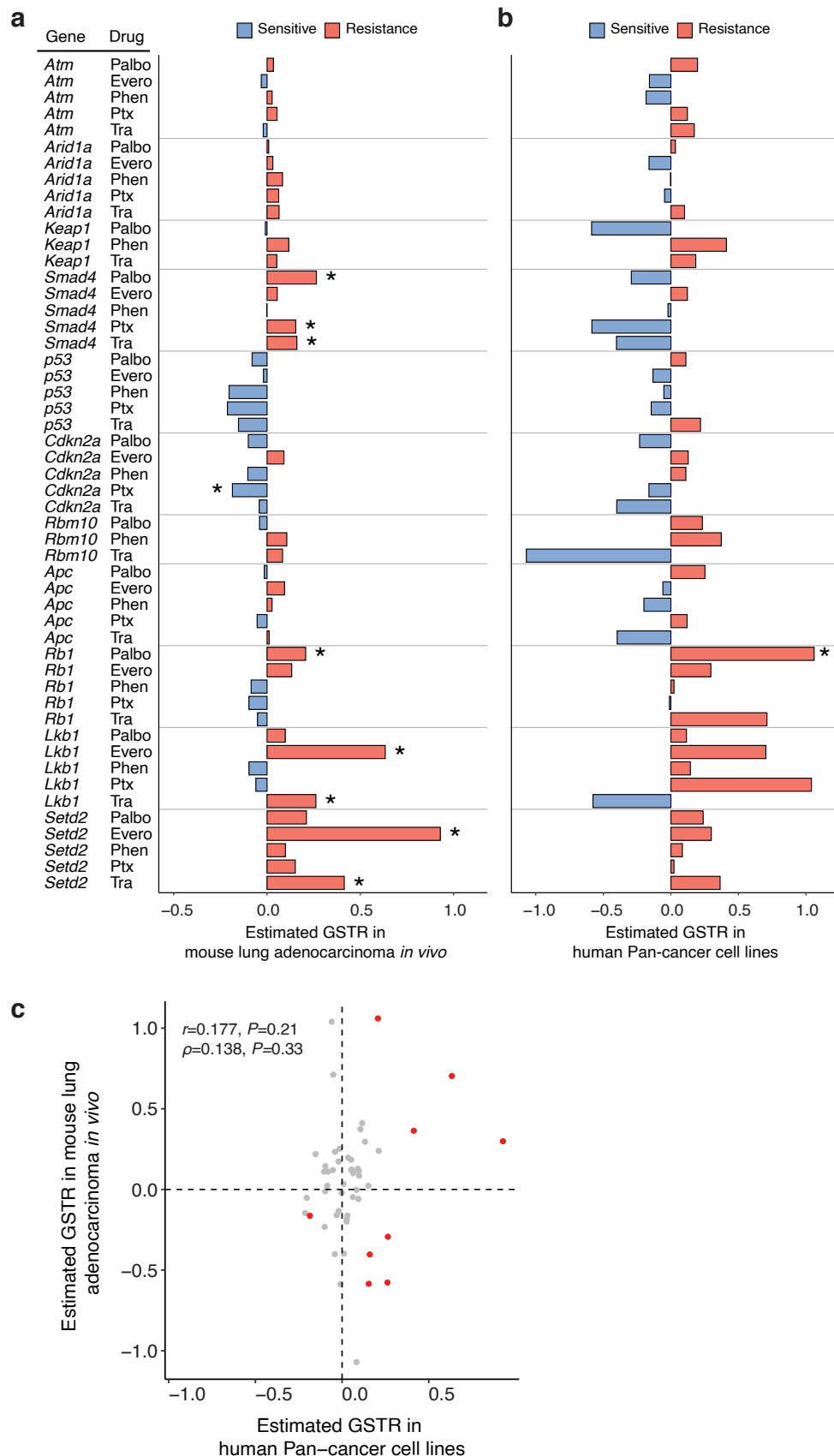
Li, Lin et al.



**Supplemental Figure 11. GSTR to Palbociclib identified in a repeat experiment.**

- Outline of the replicate experiment to identify GSTR to Palbociclib (Palbociclib repeat experiment).
- Heatmap for ScoreRTN and ScoreRGM for the Palbociclib repeat experiment. “.” indicates a marginally significant GSTR ( $P<0.1$ ), and “\*\*” indicates a significant GSTR ( $P<0.05$ ). ScoreRTN and ScoreRGM are integrated to generate  $\hat{G}$  shown in Figure 2h.
- Across two independent experiments of palbociclib, the identified genotype-specific therapy responses (GSTRs) were recaptured for both ScoreRTN (c), ScoreRGM (d), and  $\hat{G}$  (e). Large dots indicate significant GSTRs in at least one experiment, and small dots indicate that GSTR was significant in neither experiment. Pearson’s ( $r$ ) and Spearman’s correlations ( $\rho$ ) were calculated.
- Palbociclib works as a Cdk4/6 inhibitor. *Rb1* as the downstream effector is expected to be resistant to Palbociclib. *Cdkn2a* functions as a tumor suppressor upstream in the same pathway; therefore, the growth advantage conferred by the inactivation of *Cdkn2a* will be removed by the Palbociclib treatment, showing drug sensitivity. While *Rb1*-inactivation lead to significant resistance in both experiments, *Cdkn2a*-inactivation lead to marginally significant sensitivity for both ScoreRTN and ScoreRGM in the pharmacogenomic mapping experiment. Darker color intensities of Cdk4/6 represents higher activity.

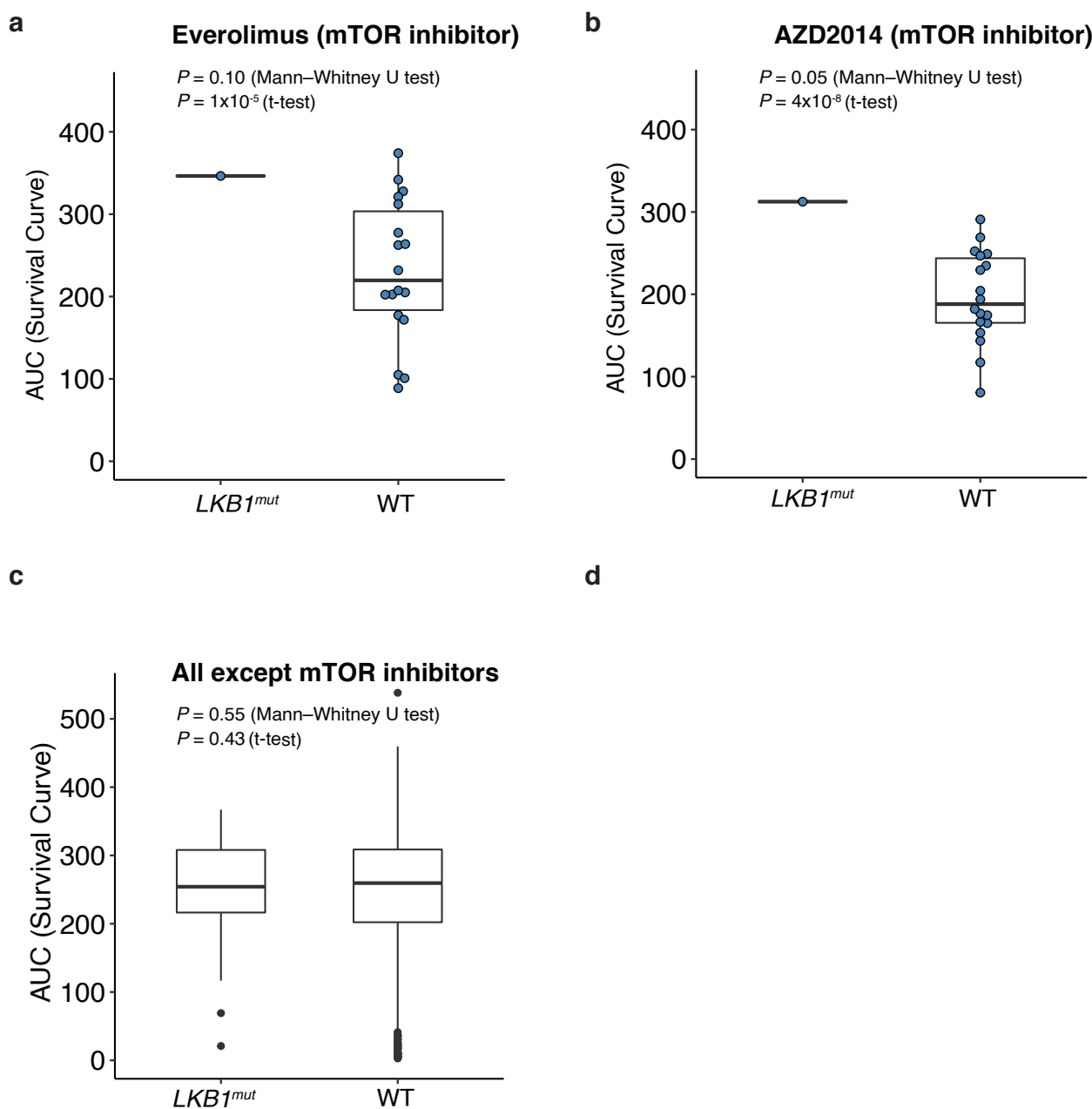
Li, Lin et al.



**Supplemental Figure 12. Comparison with the GDSC human cell line database**

- GSTR estimated from our study from mouse lung tumors *in vivo*.
- GSTR reported by GDSC for human PAN cancer cell lines. Genes are in the same order as a.
- Correlation between GSTR estimated in our study and the cancer cell line study. The significant GSTRs in our study are highlighted in red.

Li, Lin *et al.*

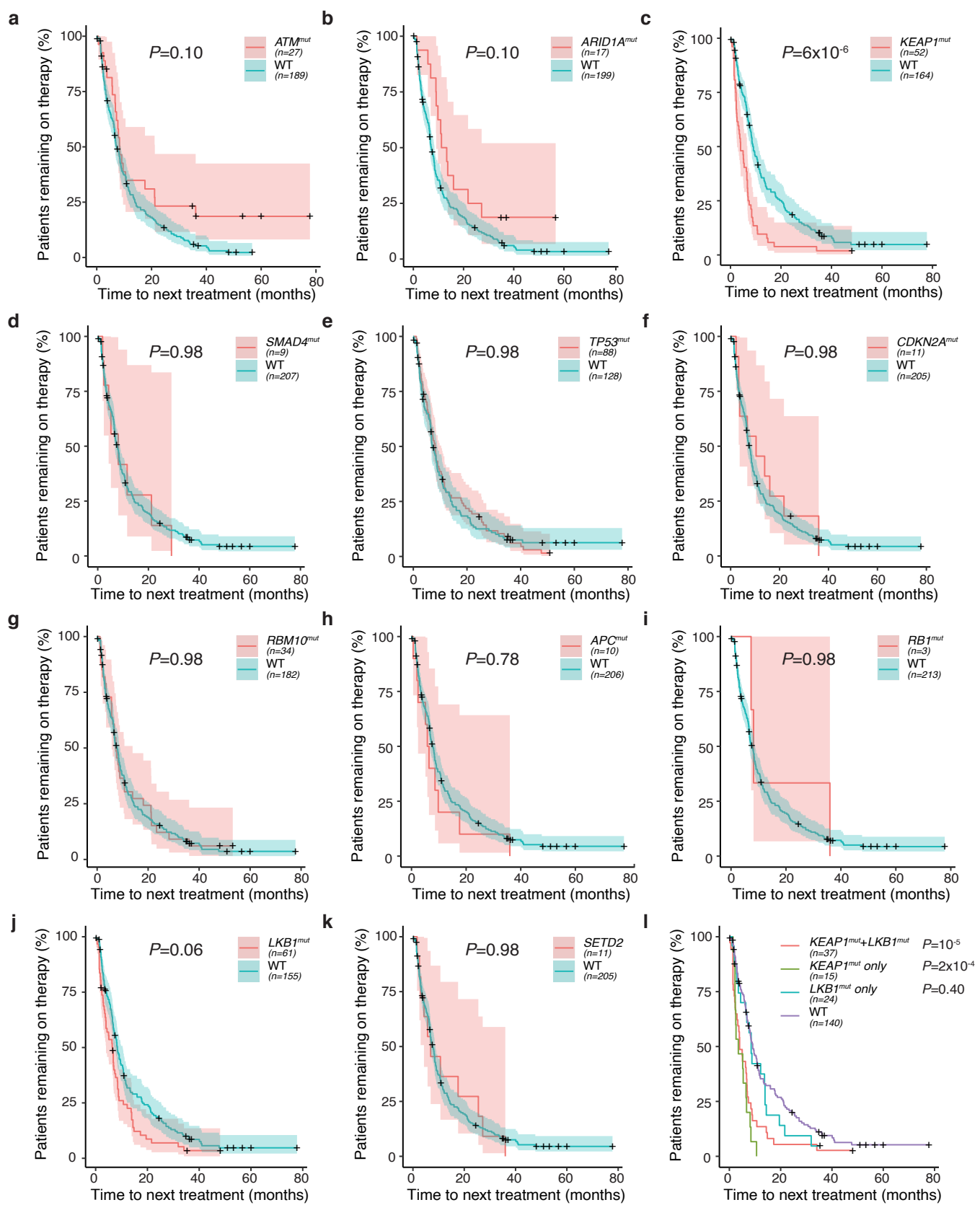


**Supplementary Figure 13. Correlation of *LKB1*-mutation with resistance to mTOR inhibition in patient-derived cancer cells from patients with lung adenocarcinoma.**

**a,b.** Jin-Ku Lee *et al.* quantified the area under the curve (AUC) of the dose-response curves as a proxy for the pharmacological responses of patient-derived cancer cells from 462 patients to 60 treatments (the Cancer-Drug eXplorer database). We focused on the 21 primary cell cultures derived from patients with lung adenocarcinomas. Among them, one had an *LKB1* mutation and those cells showed resistance to two mTOR inhibitor, everolimus (**a**), and AZD2014 (**b**). *P*-values were calculated from one-sided Mann-Whitney U-test or one-sided t-test.

**c.** The *LKB1*-mutant tumor-derived cells do not show general resistance to treatments. Another explanation for the resistance of that one sample to mTOR inhibition could be that those cancer cells (with the *LKB1* mutation) are just more resistant to therapies in general. The AUC for *LKB1* to all treatments other than mTOR inhibitors were not different from cell lines that are wild-type in *LKB1*. 985 data points were used for comparison and we did not plot individual data points for better visualization.

Li, Lin et al.



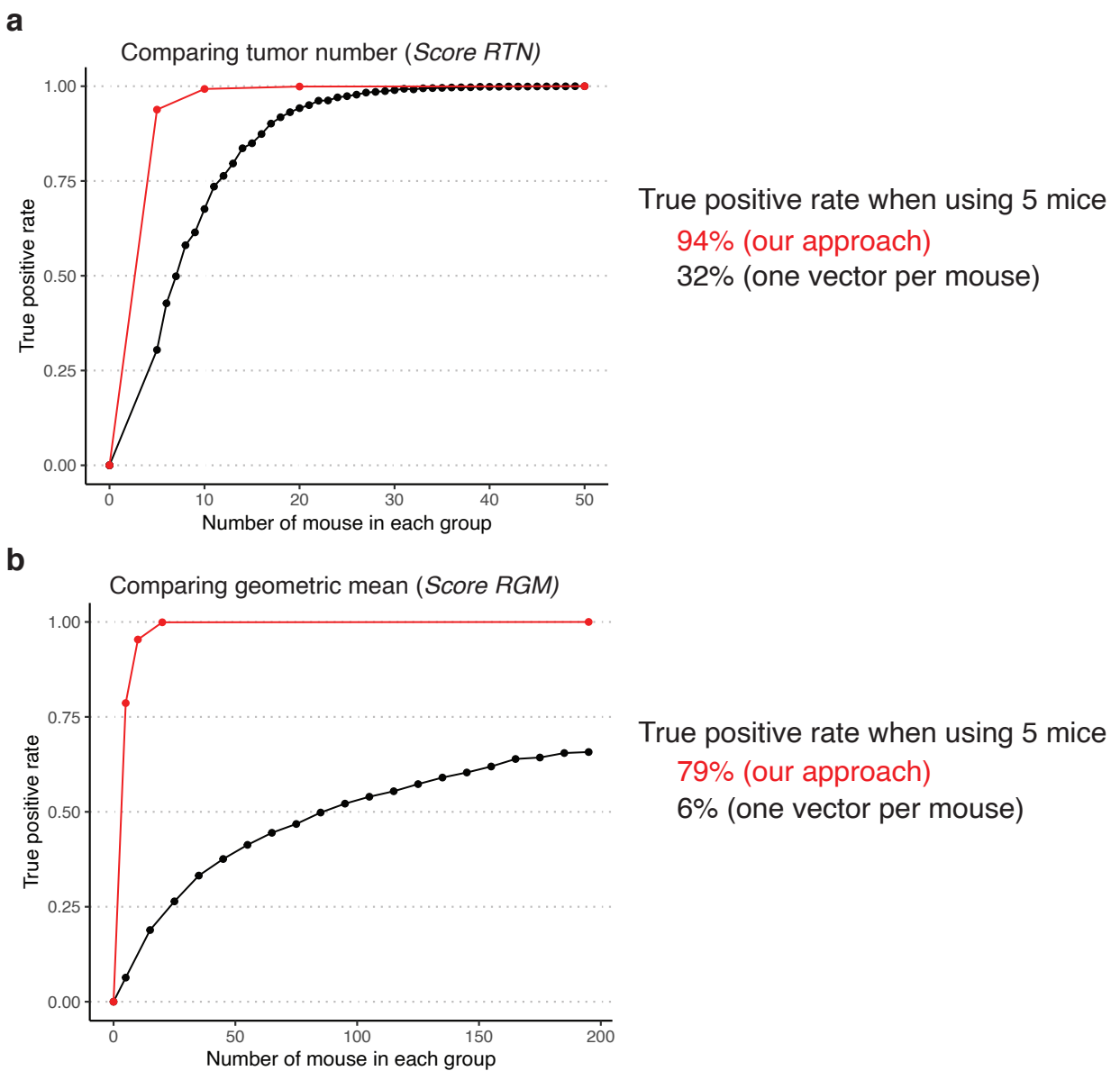
**Supplementary Figure 14. Patient response to chemotherapy represented by Kaplan–Meier estimator plot**

**a-k.** Kaplan-Meier curve (with 95% confidence interval in shading) of time-to-next-treatment (months) for patients with or without mutation of the gene of interest. Longer time-to-next-treatment is associated with better responses to chemotherapy. Here, we analyzed data from a total of 216 patients with mutations in KRAS codon 12, 13, or 16. *P*-values were calculated from the Mantel-Haenszel test with FDR correction. Genotypes compared are indicated for each plot and the number of patients in each group is shown.

**l.** *KEAP1* mutations commonly co-occur with *LKB1* mutations. We divide patients into four groups based on their mutation status of *LKB1* and *KEAP1*, and found that the nominal resistance of the *LKB1* mutant group (see Figure S13j) seems to be due to the effect of co-incident *KEAP1* mutations. Importantly, the absence of resistance conferred by *LKB1* mutation is consistent with our mouse model data. *P*-values were calculated relative to WT using the Mantel-Haenszel test with FDR correction.

Li, Lin *et al.*

## Identification of GSTR that results in tumors 50% larger than expected ( $G = +50\%$ )



**Supplementary Figure 15. The Tuba-seq platform greatly reduces the amount of work and costs for identifying genotype-specific therapeutic responses.**

**a.** The sensitivity of using our Tuba-seq method (*ScoreRTN* metric) with multiplexed vectors is higher than having one vector per mouse and comparing the number (and/or size) of tumors between untreated and treated cohorts. We performed 1000 simulations for each sample size and calculated the probability of identifying the preassigned GSTR. In our study, using five mice in each group has a high true positive rate of 94% for identifying GSTRs with  $G=+50\%$ . For the one vector per mouse approach, to achieve only a 50% true positive rate, we would need ~7 mice per vector, and a total of 672 mice (7 mice for each of the 12 genotypes under eight treatments). The cost of doing the study with one genotype per mouse would be 17-times the cost to achieve half of our true positive rate. Keep in mind that this includes a 17-fold increase in the cost of animal housing, 17-fold increase in viral vector production, 17-fold increase in the amount of each drug need, 17-fold increase in the number of mouse dosings, and 17-fold increase in the number of Tuba-seq libraries and sequencing costs. Labor-related costs would also be much higher, and the total cost of a one genotype per mouse study would exceed several million dollars. Following the same logic, to achieve a similar true positive rate of 94%, ~50 times more mice would be needed with proportional increases in all costs.

**b.** Sensitivity for using our Tuba-seq method (*ScoreRGM* metric) with multiplexed vectors is much higher than having one vector per mouse and comparing the geometric mean of tumors between the untreated and treated mice. Note that assuming uniform GSTR, the metric that compares the tumor numbers has higher statistical power than the metric comparing the geometric means, and the x-axes are plotted on different scales for better visualization. Using the size metric *ScoreRGM* alone, having five mice in each group results in a true positive rate of 79% in identifying GSTR with  $G=+50\%$ . For the one vector per mouse approach, to achieve a 50% true positive rate, we would need ~85 mice per vector, which is a total of 8160 mice for performing the pharmacogenomic mapping experiment. The total cost for a study like that would be astronomical.